

Continuous-Aperture Array (CAPA)-Based Wireless Communications: Capacity Characterization

Boqun Zhao, *Graduate Student Member, IEEE*, Chongjun Ouyang, *Member, IEEE*,
Xingqi Zhang, *Member, IEEE*, and Yuanwei Liu, *Fellow, IEEE*

Abstract—The capacity limits of continuous-aperture array (CAPA)-based wireless communications are characterized. To this end, an analytically tractable transmission framework is established for both uplink and downlink CAPA systems. Based on this framework, closed-form expressions for the single-user channel capacity are derived. The results are further extended to a multiuser case by characterizing the capacity limits of a two-user channel and proposing the associated capacity-achieving decoding and encoding schemes. 1) For the uplink case, the sum-rate capacity and capacity region, as well as the capacity-achieving detectors, are derived. 2) For the downlink case, the uplink-downlink duality is established by deriving the uplink-to-downlink and downlink-to-uplink transformations under the same power constraint, based on which the optimal power allocation policy and the achieved sum-rate capacity and capacity region are characterized. To gain further insights, several case studies are presented by specializing the derived results into various array structures, including the planar CAPA, linear CAPA, and planar spatially discrete array (SPDA). Numerical results are provided to reveal that: i) the channel capacity achieved by CAPAs converges towards a finite upper bound as the aperture size increases; and ii) CAPAs offer significant capacity gains over the conventional SPDAs.

Index Terms—Channel capacity, continuous aperture array (CAPA), performance analysis.

I. INTRODUCTION

Multiple antenna technology serves as a cornerstone in the advancement of modern wireless communication systems. At its core lies the principle of leveraging an increased number of antenna elements to enhance spatial degrees of freedom (DoFs) and augment channel capacity [2]. Traditionally, multiple antenna prototypes follow a spatially discrete topological structure, where each antenna is depicted as a distinct point [3]. Motivated by the advantages of incorporating a greater number of antennas, the concept of densely packed antennas has garnered considerable interest in the communication field.

Within a fixed array aperture, reducing the distance between elements enables the addition of more antennas, thus increasing spatial DoFs. This development has led to the emergence of holographic arrays [4], [5]. In such arrays, antenna elements

are densely packed in a configuration that is spaced less than half a wavelength apart, resulting in enhanced spectral efficiency [6].

Building on the advancements discussed, this paper introduces a novel concept in antenna design—*continuous aperture array (CAPA)*. CAPA represents a paradigm shift from the conventional spatially discrete array (SPDA), evolving towards an array that forms a spatially continuous electromagnetic (EM) aperture. Essentially, a CAPA can be envisioned as an SPDA comprising an *infinite number* of antennas with *infinitesimal spacing* [3], [7]. The concept of a CAPA marks a significant advancement towards maximizing the spatial DoFs available in antenna array configurations, thereby providing substantial gains in system performance. Transitioning from discrete to continuous aperture arrays enhances signal resolution and provides more flexible control over EM wave propagation. Through this innovative approach, CAPA paves the way for next-generation antenna technologies, promising to revolutionize wireless communication infrastructures with its advanced spatial processing capabilities [8].

However, unlike traditional arrays that are modeled using spatially discrete approaches, the modeling of CAPA-based wireless transmission introduces a fundamentally different method grounded in *EM field theory*. Specifically, while the channels of conventional SPDAs are typically represented through *discrete matrices*, the spatial response of a CAPA necessitates representation through a *continuous operator in Hilbert space* [9], [10]. This shift from discrete to continuous modeling is not merely a technical detail but a transformative change in how wireless transmission systems are understood and designed [11]. The use of continuous operators to model the spatial responses of CAPAs signifies a departure from the traditional matrix-based methods suited to SPDAs. This change is crucial because it implies that the entire framework for analyzing and designing transmissions in traditional SPDAs becomes fundamentally inapplicable to CAPAs. Consequently, new conceptual and mathematical frameworks tailored specifically to handle the continuous nature of EM field interactions within CAPAs are necessary [9], [10]. This development is essential for fully exploiting the potential of CAPAs in enhancing system performance.

Currently, research on CAPA remains in a nascent stage and is predominantly focused on single-user scenarios [11]–[15]. While these foundational studies have laid the groundwork, exploration into the performance of multiuser CAPA systems is considerably less developed. Their performance, such as channel capacity, has been seldom analyzed, with only [16] presenting some initial results. Specifically, the authors of [16]

Part of this work has been submitted to the IEEE Global Communications Conference (GLOBECOM), Cape Town, South Africa, Dec. 2024 [1].

B. Zhao and X. Zhang are with the Department of Electrical and Computer Engineering, University of Alberta, Edmonton AB, T6G 2R3, Canada (email: {boqun1, xingqi.zhang}@ualberta.ca).

C. Ouyang is with the School of Electrical and Electronic Engineering, University College Dublin, Dublin, D04 V1W8, Ireland, and also with the School of Electronic Engineering and Computer Science, Queen Mary University of London, London, E1 4NS, U.K. (e-mail: chongjun.ouyang@ucd.ie).

Y. Liu is with the School of Electronic Engineering and Computer Science, Queen Mary University of London, London, E1 4NS, U.K. (email: yuanwei.liu@qmul.ac.uk).

proposed a sophisticated channel model that utilizes a Green's function method and leverages a continuous electric current distribution. Their research also extends to the performance analysis of CAPA-based reconfigurable intelligent surfaces (RIS) and simultaneously transmitting and reflecting RISs, which provides new insights into the capabilities of CAPAs in more dynamic settings.

Despite these advancements, a significant gap remains in our understanding of the full potential of CAPAs, particularly regarding their fundamental performance limits. More importantly, an analytically tractable framework for CAPA-based communications is lacking. This framework is essential for advancing both the theoretical understanding and practical deployment of these systems. It would facilitate a deeper comprehension of CAPAs' capabilities and enable the design of more effective and efficient communication strategies tailored to their unique properties, especially in multiuser scenarios where complexity and demand for system efficiency are significantly higher.

Motivated by these knowledge gaps, this paper proposes a novel analytical framework to address the continuous nature of EM fields within CAPAs, providing a robust foundation for modeling and understanding CAPA-based communications. Using this framework, the channel capacity for both downlink and uplink CAPA-based communications is characterized. The main contributions are summarized as follows.

- We propose a transmission framework for uplink and downlink CAPA communications using EM field theories, where continuous operators model both signals and spatial responses. Based on this framework, we design optimal detectors and source current distributions to achieve the single-user channel capacity for uplink and downlink CAPA communications, and derive closed-form expressions for the corresponding channel capacity.
- We then extend our analysis to multiuser CAPA systems by studying a two-user case. For uplink CAPA communications, we propose using successive decoding to achieve capacity and derive closed-form expressions for the optimal detectors of each user. Based on this, we derive closed-form expressions for the per-user rate and the sum-rate capacity, and characterize the capacity region. For downlink CAPA communications, we establish the uplink-downlink duality by presenting the uplink-to-downlink and downlink-to-uplink transformations under the same sum power constraint and derive closed-form expressions for the capacity-achieving source current distributions. Additionally, we characterize the downlink capacity limits by deriving the per-user rate, sum-rate capacity, and capacity region.
- To unveil further system insights, we present several case studies exploring the line-of-sight (LoS) channel model. The derived results are specialized to various array structures, including the planar CAPA, linear CAPA, and planar SPDA. We derive closed-form expressions for the sum-rate capacity in each case and perform asymptotic analyses by setting the aperture size to infinity.
- We present numerical results illustrating that the capacity achieved by the CAPA increases with aperture size and

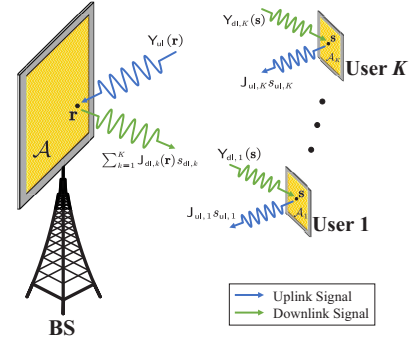


Fig. 1: Illustration of CAPA-based communications.

converges to a finite upper limit. Our results demonstrate that, compared to CAPA, the capacity of the conventional SPDA is limited by its array occupation ratio. Moreover, CAPA offers significant capacity enhancements over conventional SPDA, whose capacity converges to that of CAPA as the array occupation ratio approaches one.

The remainder of this paper is organized as follows. Section II introduces the transmission framework for CAPA-based communications. Sections III and IV delve into the capacity analysis and the capacity-achieving schemes for single-user and multiuser CAPA systems, respectively. Section V provides case studies for several specific array structures. Section VI presents numerical results to demonstrate the superior performance of CAPAs. Finally, Section VII concludes the paper.

II. SYSTEM MODEL

Consider a scenario where a base station (BS) simultaneously communicates with K users, with both the BS and each user equipped with a CAPA, as shown in Fig. 1. The aperture of the CAPA at the BS is denoted as $\mathcal{A} \subseteq \mathbb{R}^{3 \times 1}$, with an aperture size $A = \int_{\mathcal{A}} ds$. The CAPA of each user $k \in \{1, \dots, K\}$ is centered at $\mathbf{s}_k \in \mathbb{R}^{3 \times 1}$ and its aperture is denoted as $\mathcal{A}_k \subseteq \mathbb{R}^{3 \times 1}$ with a size $A_{u,k} = \int_{\mathcal{A}_k} ds$.

A. Signal Model

1) *Uplink Communications:* We commence with the uplink scenario, where the users simultaneously transmit their respective messages to the BS. Let us define $\mathbf{J}_{ul,k}(\mathbf{s}) \in \mathbb{C}$ as the continuous distribution of source currents generated by user k at point $\mathbf{s} \in \mathcal{A}_k$ to convey the normalized coded data symbol $s_{ul,k} \in \mathbb{C}$ with $\mathbb{E}\{|s_{ul,k}|^2\} = 1$. The transmitted signal by user k is thus given by $x_{ul,k}(\mathbf{s}) = \mathbf{J}_{ul,k}(\mathbf{s})s_{ul,k}$ for $\mathbf{s} \in \mathcal{A}_k$.

The excited electric field $\mathbf{E}_{ul,k}(\mathbf{r}) \in \mathbb{C}$ by user k at point $\mathbf{r} \in \mathcal{A}$ can be expressed as follows [17]:

$$\mathbf{E}_{ul,k}(\mathbf{r}) = \int_{\mathcal{A}_k} \mathbf{H}(\mathbf{r}, \mathbf{s})x_{ul,k}(\mathbf{s})ds \quad (1a)$$

$$= s_{ul,k} \int_{\mathcal{A}_k} \mathbf{H}(\mathbf{r}, \mathbf{s})\mathbf{J}_{ul,k}(\mathbf{s})ds, \quad (1b)$$

where $\mathbf{H}(\mathbf{r}, \mathbf{s}) \in \mathbb{C}$ denotes the spatial channel response from \mathbf{s} to \mathbf{r} . Given that the aperture size of each user is on the order of a wavelength in practice and is significantly smaller than the propagation distance, the variations in currents and

channel responses across the transmit aperture are negligible. Consequently, we have $H(\mathbf{r}, \mathbf{s}) \approx H(\mathbf{r}, \mathbf{s}_k) \triangleq H_k(\mathbf{r})$ and $J_{ul,k}(\mathbf{s}) \approx J_{ul,k}(\mathbf{s}_k) \triangleq J_{ul,k}$ for $\mathbf{s} \in \mathcal{A}_k$. It follows that

$$\mathbf{E}_{ul,k}(\mathbf{r}) \approx H_k(\mathbf{r}) J_{ul,k} s_{ul,k} \int_{\mathcal{A}_k} d\mathbf{s} = H_k(\mathbf{r}) J_{ul,k} A_{u,k} s_{ul,k}. \quad (2)$$

The total observed electric field $\mathbf{Y}_{ul}(\mathbf{r})$ at point $\mathbf{r} \in \mathcal{A}$ is the sum of the information-carrying electric fields $\{\mathbf{E}_{ul,k}(\mathbf{r})\}_{k=1}^K$, along with a random noise field $\mathbf{N}_{ul}(\mathbf{r}) \in \mathbb{C}$, i.e.,

$$\mathbf{Y}_{ul}(\mathbf{r}) = \sum_{k=1}^K \mathbf{E}_{ul,k}(\mathbf{r}) + \mathbf{N}_{ul}(\mathbf{r}) \quad (3a)$$

$$\approx \sum_{k=1}^K H_k(\mathbf{r}) J_{ul,k} A_{u,k} s_{ul,k} + \mathbf{N}_{ul}(\mathbf{r}), \quad (3b)$$

where $\mathbf{N}_{ul}(\mathbf{r})$ accounts for thermal noise [18]. The noise field is modeled as a zero-mean complex Gaussian random process satisfying $\mathbb{E}\{\mathbf{N}_{ul}(\mathbf{r})\mathbf{N}_{ul}^*(\mathbf{r}')\} = \sigma^2 \delta(\mathbf{r} - \mathbf{r}')$ [18], where $\delta(\cdot)$ represents the Dirac delta function, and σ^2 describes the noise intensity. $\mathbf{N}_{ul}(\mathbf{r})$ and $\{s_{ul,k}\}_{k=1}^K$ are assumed to be uncorrelated. After observing $\mathbf{Y}_{ul}(\mathbf{r})$, the BS should employ a properly designed detector along with maximum-likelihood (ML) decoding to recover the data information encoded in $\{s_{ul,k}\}_{k=1}^K$, which will be detailed in Section III-A.

2) *Downlink Communications*: At the BS, the downlink electrical signal is designed as follows:

$$x_{dl}(\mathbf{r}) = \sum_{k=1}^K J_{dl,k}(\mathbf{r}) s_{dl,k} \quad (4)$$

where $s_{dl,k} \in \mathbb{C}$ represents the coded data symbol dedicated to user k with $\mathbb{E}\{|s_{dl,k}|^2\} = 1$, and $J_{dl,k}(\mathbf{r}) \in \mathbb{C}$ ($\mathbf{r} \in \mathcal{A}$) is the associated current distribution to convey $s_{dl,k}$. As a result, the excited electric field at point $\mathbf{s} \in \mathcal{A}_k$ within user k 's aperture can be written as $\mathbf{E}_{dl,k}(\mathbf{s}) = \int_{\mathcal{A}} H(\mathbf{s}, \mathbf{r}) x_{dl}(\mathbf{r}) d\mathbf{r}$, viz.

$$\mathbf{E}_{dl,k}(\mathbf{s}) = \int_{\mathcal{A}} H(\mathbf{s}, \mathbf{r}) \left(\sum_{k'=1}^K J_{dl,k'}(\mathbf{r}) s_{dl,k'} \right) d\mathbf{r}. \quad (5)$$

Since the aperture size of each user is generally negligible with respect to both the propagation distance and the BS aperture size, the variations of the electric field and channel response along the receive aperture can be omitted. This yields $\mathbf{E}_{dl,k}(\mathbf{s}) \approx \mathbf{E}_{dl,k}(\mathbf{s}_k) \triangleq \mathbf{E}_{dl,k}$ and $H(\mathbf{s}, \mathbf{r}) \approx H(\mathbf{s}_k, \mathbf{r}) = H(\mathbf{r}, \mathbf{s}_k) = H_k(\mathbf{r})$ for $\mathbf{s} \in \mathcal{A}_k$. Therefore, we obtain

$$\mathbf{E}_{dl,k}(\mathbf{s}) \approx \mathbf{E}_{dl,k} = \int_{\mathcal{A}} H_k(\mathbf{r}) \left(\sum_{k'=1}^K J_{dl,k'}(\mathbf{r}) s_{dl,k'} \right) d\mathbf{r}. \quad (6)$$

Accordingly, the observation of user k at point $\mathbf{s} \in \mathcal{A}_k$ can be written as follows:

$$\mathbf{Y}_{dl,k}(\mathbf{s}) = \mathbf{E}_{dl,k}(\mathbf{s}) + \mathbf{N}_{dl,k}(\mathbf{s}) \approx \mathbf{E}_{dl,k} + \mathbf{N}_{dl,k}(\mathbf{s}) \quad (7a)$$

$$\begin{aligned} &= s_{dl,k} \int_{\mathcal{A}} H_k(\mathbf{r}) J_{dl,k}(\mathbf{r}) d\mathbf{r} + \mathbf{N}_{dl,k}(\mathbf{s}) \\ &+ \sum_{k' \neq k} s_{dl,k'} \int_{\mathcal{A}} H_k(\mathbf{r}) J_{dl,k'}(\mathbf{r}) d\mathbf{r}, \end{aligned} \quad (7b)$$

where $\mathbf{N}_{dl,k}(\mathbf{s})$ denotes the thermal noise subject to $\mathbb{E}\{\mathbf{N}_{dl,k}(\mathbf{s})\mathbf{N}_{dl,k}^*(\mathbf{s}')\} = \sigma_k^2 \delta(\mathbf{s} - \mathbf{s}')$.

B. Channel Model

To facilitate theoretical investigations into fundamental performance limits and asymptotic behaviors, we focus our dis-

cussion on LoS channels. Under this consideration, $H(\mathbf{r}, \mathbf{s})$ is modeled as follows [19]:

$$H(\mathbf{r}, \mathbf{s}) = H^{\text{em}}(\mathbf{r}, \mathbf{s}) H^{\text{pa}}(\mathbf{r}, \mathbf{s}), \quad (8)$$

where $H^{\text{pa}}(\mathbf{r}, \mathbf{s}) \triangleq \sqrt{\frac{|\mathbf{e}^T(\mathbf{s} - \mathbf{r})|}{\|\mathbf{r} - \mathbf{s}\|}}$ models the impact of the projected aperture of the BS array, and where $\mathbf{e} \in \mathbb{R}^{3 \times 1}$ is the normal vector of the CAPA at the BS. We comment that the projected aperture is reflected by the projection of the normal vector onto the wave propagation direction. Furthermore, the function

$$H^{\text{em}}(\mathbf{r}, \mathbf{s}) \triangleq \frac{jk_0 \eta e^{-jk_0 \|\mathbf{r} - \mathbf{s}\|}}{4\pi \|\mathbf{r} - \mathbf{s}\|} \left(1 + \frac{jk_0^{-1}}{\|\mathbf{r} - \mathbf{s}\|} - \frac{k_0^{-2}}{\|\mathbf{r} - \mathbf{s}\|^2} \right) \quad (9)$$

models the influence of free-space EM propagation, where $\eta = 120\pi$ is the impedance of free space, and $k_0 = \frac{2\pi}{\lambda}$ with λ being the wavelength denotes the wavenumber. Particularly, $H^{\text{em}}(\mathbf{r}, \mathbf{s})$ comprises three terms: the first term corresponds to the radiating near-field and far-field regions, while the remaining two terms correspond to the reactive near-field region. The squared magnitude of the parenthesis in (9) is $1 - \frac{k_0^{-2}}{\|\mathbf{r} - \mathbf{s}\|^2} + \frac{k_0^{-4}}{\|\mathbf{r} - \mathbf{s}\|^4}$, which equals 0.97 at distance $\|\mathbf{r} - \mathbf{s}\| = \lambda$ [19]. Hence, when considering practical systems with $\|\mathbf{r} - \mathbf{s}\| \gg \lambda$, the last two terms in (9) can be neglected. As a result, (9) is approximated as follows:

$$H^{\text{em}}(\mathbf{r}, \mathbf{s}) \approx \frac{jk_0 \eta}{4\pi \|\mathbf{r} - \mathbf{s}\|} e^{-jk_0 \|\mathbf{r} - \mathbf{s}\|}. \quad (10)$$

III. SINGLE-USER CASE

Having established the system model, we first characterize the channel capacity of CAPA-based single-user communications. For $K = 1$, we omit the user index k in the subscripts and denote $\mathcal{A}_u \subseteq \mathbb{R}^{3 \times 1}$, $\mathbf{s}_u \in \mathbb{R}^{3 \times 1}$, and A_u as the user's array aperture, its center location, and aperture size, respectively.

A. Uplink Capacity

We commence with the uplink scenario. In the single-user case, (3b) simplifies to

$$\mathbf{Y}_{ul}(\mathbf{r}) = H(\mathbf{r}) J_{ul} A_u s_{ul} + \mathbf{N}_{ul}(\mathbf{r}). \quad (11)$$

We then design a detector $\mathbf{V}_{ul}(\mathbf{r})$ to recover s_{ul} from $\mathbf{Y}_{ul}(\mathbf{r})$. Specifically, applying this detector to $\mathbf{Y}_{ul}(\mathbf{r})$ yields

$$\begin{aligned} \int_{\mathcal{A}} \mathbf{V}_{ul}^*(\mathbf{r}) \mathbf{Y}_{ul}(\mathbf{r}) d\mathbf{r} &= s_{ul} J_{ul} A_u \int_{\mathcal{A}} \mathbf{V}_{ul}^*(\mathbf{r}) H(\mathbf{r}) d\mathbf{r} \\ &+ \int_{\mathcal{A}} \mathbf{V}_{ul}^*(\mathbf{r}) \mathbf{N}_{ul}(\mathbf{r}) d\mathbf{r}. \end{aligned} \quad (12)$$

Since $\mathbf{N}_{ul}(\mathbf{r})$ is a zero-mean complex Gaussian random field, $\int_{\mathcal{A}} \mathbf{V}_{ul}^*(\mathbf{r}) \mathbf{N}_{ul}(\mathbf{r}) d\mathbf{r}$ is complex Gaussian distributed. Its mean and variance are calculated as follows.

Lemma 1. Under the assumption that $\mathbf{N}_{ul}(\mathbf{r})$ is a zero-mean complex Gaussian process with $\mathbb{E}\{\mathbf{N}_{ul}(\mathbf{r})\mathbf{N}_{ul}^*(\mathbf{r}')\} = \sigma^2 \delta(\mathbf{r} - \mathbf{r}')$, we have $\int_{\mathcal{A}} \mathbf{V}_{ul}^*(\mathbf{r}) \mathbf{N}_{ul}(\mathbf{r}) d\mathbf{r} \sim \mathcal{CN}(0, \sigma^2 \int_{\mathcal{A}} |\mathbf{V}_{ul}(\mathbf{r})|^2 d\mathbf{r})$.

Proof: Please refer to Appendix A for more details. ■

The signal-to-noise ratio (SNR) for decoding s_{ul} is thus given by

$$\gamma_{ul} = \frac{A_u^2 |J_{ul}|^2 \left| \int_{\mathcal{A}} \mathbf{V}_{ul}^*(\mathbf{r}) \mathbf{H}(\mathbf{r}) d\mathbf{r} \right|^2}{\sigma^2 \int_{\mathcal{A}} |\mathbf{V}_{ul}(\mathbf{r})|^2 d\mathbf{r}}. \quad (13)$$

The subsequent task is to design $\mathbf{V}_{ul}(\mathbf{r})$ to maximize γ_{ul} . As observed from (13), γ_{ul} is independent of the norm of $\mathbf{V}_{ul}(\mathbf{r})$, i.e., $\int_{\mathcal{A}} |\mathbf{V}_{ul}(\mathbf{r})|^2 d\mathbf{r}$. Thus, the optimal detector satisfies

$$\mathbf{V}_{ul}^*(\mathbf{r}) \propto \underset{\int_{\mathcal{A}} |\mathbf{V}_{ul}(\mathbf{r})|^2 d\mathbf{r} = 1}{\operatorname{argmax}} \left| \int_{\mathcal{A}} \mathbf{V}_{ul}^*(\mathbf{r}) \mathbf{H}(\mathbf{r}) d\mathbf{r} \right|^2 = \frac{\mathbf{H}(\mathbf{r})}{h_u^{1/2}}, \quad (14)$$

where $h_u \triangleq \int_{\mathcal{A}} |\mathbf{H}(\mathbf{r})|^2 d\mathbf{r}$.

Remark 1. The results in (14) suggest that the capacity-achieving detector for uplink single-user CAPA communications aligns with the spatial channel response $\mathbf{H}(\mathbf{r})$, which can be regarded as the continuous version of *maximal-ratio combining (MRC)*.

Substituting (14) back into (13) gives

$$\gamma_{ul} = \frac{A_u^2 |J_{ul}|^2}{\sigma^2} \int_{\mathcal{A}} |\mathbf{H}(\mathbf{r})|^2 d\mathbf{r} = \bar{\gamma}_{ul} \int_{\mathcal{A}} |\mathbf{G}(\mathbf{r})|^2 d\mathbf{r}, \quad (15)$$

where $\bar{\gamma}_{ul} = \frac{A_u^2 |J_{ul}|^2 k_0^2 \eta^2}{4\pi\sigma^2}$ and $\mathbf{G}(\mathbf{r}) = \frac{e^{-jk_0 \|\mathbf{r}-\mathbf{s}_{ul}\|}}{\sqrt{4\pi \|\mathbf{r}-\mathbf{s}_{ul}\|}} \sqrt{\frac{e^{\mathbf{T}(\mathbf{s}_{ul}-\mathbf{r})}}{\|\mathbf{r}-\mathbf{s}_{ul}\|}}$.

Note that $\frac{e^{-jk_0 \|\mathbf{r}-\mathbf{s}_{ul}\|}}{\sqrt{4\pi \|\mathbf{r}-\mathbf{s}_{ul}\|}}$ and $\sqrt{\frac{e^{\mathbf{T}(\mathbf{s}_{ul}-\mathbf{r})}}{\|\mathbf{r}-\mathbf{s}_{ul}\|}}$ characterize the impact of spherical-wave propagation and projected aperture in arbitrary homogeneous mediums, respectively. Thus, we define $\int_{\mathcal{A}} |\mathbf{G}(\mathbf{r})|^2 d\mathbf{r} \triangleq \mathbf{g}_u$ as the channel gain. The remaining term $\bar{\gamma}_{ul}$ can be treated as the uplink transmit SNR. As a result, building upon (15), the single-user uplink channel capacity can be written as follows:

$$C_{ul} = \log_2(1 + \gamma_{ul}) = \log_2(1 + \bar{\gamma}_{ul} \mathbf{g}_u). \quad (16)$$

B. Downlink Capacity

Turning to the downlink case, for $K = 1$, (7b) simplifies to

$$\mathbf{Y}_{dl}(\mathbf{s}) = s_{dl} \int_{\mathcal{A}} \mathbf{H}(\mathbf{r}) \mathbf{J}_{dl}(\mathbf{r}) d\mathbf{r} + \mathbf{N}_{dl}(\mathbf{s}), \quad (17)$$

where $\mathbb{E}\{\mathbf{N}_{dl}(\mathbf{s}) \mathbf{N}_{dl}^*(\mathbf{s}')\} = \sigma_u^2 \delta(\mathbf{s} - \mathbf{s}')$. Applying the detector $\mathbf{V}_{dl}(\mathbf{s})$ to $\mathbf{Y}_{dl}(\mathbf{s})$ yields

$$\begin{aligned} \int_{\mathcal{A}_u} \mathbf{V}_{dl}^*(\mathbf{s}) \mathbf{Y}_{dl}(\mathbf{s}) d\mathbf{s} &= s_{dl} \int_{\mathcal{A}} \mathbf{H}(\mathbf{r}) \mathbf{J}_{dl}(\mathbf{r}) d\mathbf{r} \int_{\mathcal{A}_u} \mathbf{V}_{dl}^*(\mathbf{s}) d\mathbf{s} \\ &+ \int_{\mathcal{A}_u} \mathbf{V}_{dl}^*(\mathbf{s}) \mathbf{N}_{dl}(\mathbf{s}) d\mathbf{s}. \end{aligned} \quad (18)$$

Similar to **Lemma 1**, we have $\int_{\mathcal{A}_u} \mathbf{V}_{dl}^*(\mathbf{s}) \mathbf{N}_{dl}(\mathbf{s}) d\mathbf{s} \sim \mathcal{CN}(0, \sigma_u^2 \int_{\mathcal{A}_u} |\mathbf{V}_{dl}(\mathbf{s})|^2 d\mathbf{s})$. As a result, the SNR for decoding s_{dl} is given by

$$\gamma_{dl} = \frac{\left| \int_{\mathcal{A}_u} \mathbf{V}_{dl}^*(\mathbf{s}) d\mathbf{s} \right|^2 \left| \int_{\mathcal{A}} \mathbf{H}(\mathbf{r}) \mathbf{J}_{dl}(\mathbf{r}) d\mathbf{r} \right|^2}{\sigma_u^2 \int_{\mathcal{A}_u} |\mathbf{V}_{dl}(\mathbf{s})|^2 d\mathbf{s}}. \quad (19)$$

By noting that A_u is negligible with respect to the propagation distance, we have

$$\int_{\mathcal{A}_u} \mathbf{V}_{dl}^*(\mathbf{s}) d\mathbf{s} \approx \mathbf{V}_{dl}^*(\mathbf{s}_u) A_u, \quad \int_{\mathcal{A}_u} |\mathbf{V}_{dl}(\mathbf{s})|^2 d\mathbf{s} \approx |\mathbf{V}_{dl}(\mathbf{s}_u)|^2 A_u,$$

which simplifies (19) as follows:

$$\gamma_{dl} \approx \frac{|\mathbf{V}_{dl}^*(\mathbf{s}_u)|^2 A_u^2 \left| \int_{\mathcal{A}} \mathbf{H}(\mathbf{r}) \mathbf{J}_{dl}(\mathbf{r}) d\mathbf{r} \right|^2}{\sigma_u^2 |\mathbf{V}_{dl}(\mathbf{s}_u)|^2 A_u} \quad (20a)$$

$$= \frac{A_u \left| \int_{\mathcal{A}} \mathbf{H}(\mathbf{r}) \mathbf{J}_{dl}(\mathbf{r}) d\mathbf{r} \right|^2}{\sigma_u^2}. \quad (20b)$$

The results in (20b) suggest that the downlink SNR is independent of the detector $\mathbf{V}_{dl}(\mathbf{s})$ under our settings. Thus, any detector can be used to recover s_{dl} . Additionally, from (20b), it is observed that the SNR is maximized when the current distribution satisfies $\mathbf{J}_{dl}(\mathbf{r}) \propto \mathbf{H}^*(\mathbf{r})$, i.e.,

$$\mathbf{J}_{dl}(\mathbf{r}) = \frac{\mathbf{H}^*(\mathbf{r})}{h_u^{1/2}} \sqrt{\int_{\mathcal{A}} |\mathbf{J}_{dl}(\mathbf{r})|^2 d\mathbf{r}}, \quad (21)$$

where $\int_{\mathcal{A}} |\mathbf{J}_{dl}(\mathbf{r})|^2 d\mathbf{r}$ is proportional to the transmit power.

Remark 2. The results in (21) suggest that the capacity-achieving source current for downlink single-user CAPA communications aligns with $\mathbf{H}(\mathbf{r})$, which can be regarded as the continuous version of *maximal-ratio transmission (MRT)*.

Inserting (21) into (20b) gives

$$\gamma_{dl} = \frac{A_u \int_{\mathcal{A}} |\mathbf{J}_{dl}(\mathbf{r})|^2 d\mathbf{r}}{\sigma_u^2} \int_{\mathcal{A}} |\mathbf{H}(\mathbf{r})|^2 d\mathbf{r} = \bar{\gamma}_{dl} \mathbf{g}_u, \quad (22)$$

where $\bar{\gamma}_{dl} = \frac{A_u \int_{\mathcal{A}} |\mathbf{J}_{dl}(\mathbf{r})|^2 d\mathbf{r} k_0^2 \eta^2}{4\pi\sigma_u^2}$ can be interpreted as the downlink transmit SNR. Based on (22), the single-user downlink capacity is given by

$$C_{dl} = \log_2(1 + \gamma_{dl}) = \log_2(1 + \bar{\gamma}_{dl} \mathbf{g}_u). \quad (23)$$

IV. MULTIUSER CASE

This section extends the single-user scenario to the multiuser one. We characterize the channel capacity for both uplink and downlink communications. For brevity, our analysis focuses on the two-user case, while extensions to scenarios with an arbitrary number of users will be addressed in future work.

A. Uplink Capacity

We first analyze the uplink scenario.

1) *Optimal Uplink Detection:* When $K = 2$, the observed electric field in (3b) is given by

$$\mathbf{Y}_{ul}(\mathbf{r}) = \mathbf{H}_1(\mathbf{r}) \mathbf{J}_{ul,1} A_{u,1} s_{ul,1} + \mathbf{H}_2(\mathbf{r}) \mathbf{J}_{ul,2} A_{u,2} s_{ul,2} + \mathbf{N}_{ul}(\mathbf{r}). \quad (24)$$

The capacity of an uplink multiuser channel can be achieved using *successive interference cancellation (SIC) decoding* [2]. Specifically, the message sent by one user is first decoded by treating the message from the other user as interference. Once decoded, this interference is removed, and the other message is then decoded without inter-user interference (IUI).

Given the uplink signal model in (24), there are two possible SIC orders: $1 \rightarrow 2$ and $2 \rightarrow 1$. Here, we discuss the channel capacity achieved by the decoding order $2 \rightarrow 1$. In this case, $s_{ul,2}$ is decoded from $\mathbf{Y}_{ul}(\mathbf{r})$ by treating $\mathbf{H}_1(\mathbf{r}) \mathbf{J}_{ul,1} A_{u,1} s_{ul,1}$ as interference. After $s_{ul,2}$ is decoded and subtracted from $\mathbf{Y}_{ul}(\mathbf{r})$, $s_{ul,1}$ is decoded without IUI from the following signal:

$$\mathbf{Z}(\mathbf{r}) \triangleq \mathbf{H}_1(\mathbf{r}) \mathbf{J}_{ul,1} A_{u,1} s_{ul,1} + \mathbf{N}_{ul}(\mathbf{r}), \quad (25)$$

which is the same as that given in (11). Following the derivation steps to obtain (14), the BS can use the detector $V_{ul,1}(\mathbf{r}) = \frac{H_1(\mathbf{r})}{\sqrt{\int_{\mathcal{A}} |H_1(\mathbf{r})|^2 d\mathbf{r}}}$ to recover $s_{ul,1}$ from (25). Therefore, the SNR for decoding the message sent by user 1 is given by

$$\gamma_{ul,1} = \bar{\gamma}_{ul,1} \mathbf{g}_1, \quad (26)$$

where $\bar{\gamma}_{ul,k} = \frac{A_{u,k}^2 |J_{ul,k}|^2 k_0^2 \eta^2}{4\pi\sigma^2}$ denotes the transmit SNR of user $k \in \{1, 2\}$, and $\mathbf{g}_k = \int_{\mathcal{A}} |G_k(\mathbf{r})|^2 d\mathbf{r}$ denotes the associated channel gain with $G_k(\mathbf{r}) = \frac{e^{-jk_0 \|\mathbf{r}-\mathbf{s}_k\|}}{\sqrt{4\pi\|\mathbf{r}-\mathbf{s}_k\|}} \sqrt{\frac{|e^{\mathbf{T}(\mathbf{s}_k-\mathbf{r})}|}{\|\mathbf{r}-\mathbf{s}_k\|}}$.

Next, we investigate the decoding of $s_{ul,2}$ from $Y_{ul}(\mathbf{r})$, where the interference-plus-noise term is given by $Z(\mathbf{r})$ as shown in (25). Since $N_{ul}(\mathbf{r})$ and $s_{ul,1}$ are uncorrelated, the autocorrelation function of the random field $Z(\mathbf{r})$ is given by

$$\begin{aligned} \mathbb{E}\{Z(\mathbf{r})Z^*(\mathbf{r}')\} &= \mathbf{G}_1(\mathbf{r})\mathbf{G}_1^*(\mathbf{r}')\bar{\gamma}_{ul,1}\sigma^2 \\ &+ \sigma^2\delta(\mathbf{r}-\mathbf{r}') \triangleq \mathbf{R}_Z(\mathbf{r},\mathbf{r}'). \end{aligned} \quad (27)$$

To obtain the optimal detector that maximizes the achievable rate of user 2, we first need to design an invertible linear transformation $W_Z(\mathbf{r}',\mathbf{r})$ to whiten $Z(\mathbf{r})$. This transformation $W_Z(\mathbf{r}',\mathbf{r})$ must satisfy the following two conditions:

i) *Whitening*: The autocorrelation function of $Z_w(\mathbf{r}') \triangleq \int_{\mathcal{A}} W_Z(\mathbf{r}',\mathbf{r})Z(\mathbf{r})d\mathbf{r}$ is proportional to the Dirac delta function, i.e.,

$$\mathbb{E}\{Z_w(\mathbf{r})Z_w^*(\mathbf{r}')\} \propto \delta(\mathbf{r}'-\mathbf{r}); \quad (28)$$

ii) *Invertibility*: Given an arbitrary function $f(\mathbf{r})$ defined on $\mathbf{r} \in \mathcal{A}$, there exists a transformation $\bar{W}_Z(\mathbf{x},\mathbf{r}')$ such that

$$\int_{\mathcal{A}} \bar{W}_Z(\mathbf{x},\mathbf{r}') \int_{\mathcal{A}} W_Z(\mathbf{r}',\mathbf{r})f(\mathbf{r})d\mathbf{r}d\mathbf{r}' = f(\mathbf{x}). \quad (29)$$

Applying an invertible transformation to $Y_{ul}(\mathbf{r})$ is information lossless and has no impact on the channel capacity [2]. To proceed, we introduce the following lemmas.

Lemma 2. The invertible linear transformation used to whiten the interference-plus-noise term $Z(\mathbf{r})$ is given by

$$W_Z(\mathbf{r}',\mathbf{r}) = \delta(\mathbf{r}'-\mathbf{r}) + \mu_1 \mathbf{G}_1(\mathbf{r}')\mathbf{G}_1^*(\mathbf{r}), \quad (30)$$

where $\mu_1 = -\frac{1}{\mathbf{g}_1} \pm \frac{1}{\mathbf{g}_1\sqrt{1+\bar{\gamma}_{ul,1}\mathbf{g}_1}}$. The autocorrelation function of $Z_w(\cdot)$ satisfies $\mathbb{E}\{Z_w(\mathbf{r})Z_w^*(\mathbf{r}')\} = \sigma^2\delta(\mathbf{r}-\mathbf{r}')$. Additionally, the inversion of $W_Z(\mathbf{r}',\mathbf{r})$ is given by $\bar{W}_Z(\mathbf{r},\mathbf{r}') = \delta(\mathbf{r}-\mathbf{r}') - \frac{\mu_1}{1+\mu_1\mathbf{g}_1} \mathbf{G}_1(\mathbf{r})\mathbf{G}_1^*(\mathbf{r}')$.

Proof: Please refer to Appendix B for more details. ■

Next, we exploit $W_Z(\mathbf{r}',\mathbf{r})$ to transform $Y_B(\mathbf{r})$ as follows:

$$\int_{\mathcal{A}} W_Z(\mathbf{r}',\mathbf{r})Y_{ul}(\mathbf{r})d\mathbf{r} = \bar{H}_2(\mathbf{r}')J_{ul,2}A_{u,2}s_{ul,2} + Z_w(\mathbf{r}'), \quad (31)$$

where $\bar{H}_2(\mathbf{r}') \triangleq \int_{\mathcal{A}} W_Z(\mathbf{r}',\mathbf{r})H_2(\mathbf{r})d\mathbf{r}$. By noting that $\mathbb{E}\{Z_w(\mathbf{r})Z_w^*(\mathbf{r}')\} = \sigma^2\delta(\mathbf{r}-\mathbf{r}')$, the model presented in (31) is similar to that in (11). Motivated by this, we design an MRC-based detector $V_{ul,2}(\mathbf{r}')$ by treating $\bar{H}_2(\mathbf{r}')$ as the equivalent channel response, which yields

$$V_{ul,2}(\mathbf{r}') = \frac{\bar{H}_2(\mathbf{r}')}{\sqrt{\int_{\mathcal{A}} |\bar{H}_2(\mathbf{r}')|^2 d\mathbf{r}}}. \quad (32)$$

Following the derivation steps to obtain (15), the SNR for

<p>1: Whiten the interference-plus-noise term $Z(\mathbf{r})$:</p> $\int_{\mathcal{A}} W_Z(\mathbf{r}',\mathbf{r})Y_{ul}(\mathbf{r})d\mathbf{r} = \bar{H}_2(\mathbf{r}')J_{ul,2}A_{u,2}s_{ul,2} + Z_w(\mathbf{r}');$ <p>2: Use the MRC detector and ML decoder to recover $s_{ul,2}$:</p> $\int_{\mathcal{A}} V_{ul,2}^*(\mathbf{r}') \int_{\mathcal{A}} W_Z(\mathbf{r}',\mathbf{r})Y_{ul}(\mathbf{r})d\mathbf{r}d\mathbf{r}' \rightarrow s_{ul,2};$ <p>3: Employ SIC to subtract $H_2(\mathbf{r})J_{ul,2}A_{u,2}s_{ul,2}$ from $Y_{ul}(\mathbf{r})$;</p> <p>4: Use the MRC detector and ML decoder to recover $s_{ul,1}$:</p> $\int_{\mathcal{A}} V_{ul,1}^*(\mathbf{r})(H_1(\mathbf{r})J_{ul,1}A_{u,1}s_{ul,1} + N_{ul}(\mathbf{r}))d\mathbf{r} \rightarrow s_{ul,1}.$

TABLE I: SIC decoding for uplink CAPA communications.

decoding $s_{ul,2}$ can be written as follows:

$$\gamma_{ul,2} = \frac{A_{u,2}^2 |J_{ul,2}|^2}{\sigma^2} \int_{\mathcal{A}} |\bar{H}_2(\mathbf{r}')|^2 d\mathbf{r}'. \quad (33)$$

A closed-form expression for $\gamma_{ul,2}$ is given as follows.

Theorem 1. By first whitening $Z(\mathbf{r})$ with $W_Z(\mathbf{r}',\mathbf{r})$ and then employing the MRC detector $V_{ul,2}(\mathbf{r}')$, the resultant SNR in decoding $s_{ul,2}$ can be written as follows:

$$\gamma_{ul,2} = \bar{\gamma}_{ul,2}\mathbf{g}_2(1 - \bar{\gamma}_{ul,1}\mathbf{g}_1|\rho|^2(1 + \bar{\gamma}_{ul,1}\mathbf{g}_1)^{-1}), \quad (34)$$

where $\rho \triangleq \frac{\int_{\mathcal{A}} G_1^*(\mathbf{r})G_2(\mathbf{r})d\mathbf{r}}{\sqrt{\mathbf{g}_1\mathbf{g}_2}}$ is defined as the channel correlation factor with $|\rho| \in [0, 1]$.

Proof: Please refer to Appendix C for more details. ■

After obtaining the capacity-achieving detectors under the SIC order $2 \rightarrow 1$, we summarize the entire decoding procedure in Table I for ease of reference. The presented decoding procedure can be directly extended to the other SIC order $1 \rightarrow 2$ by *exchanging the user indices*.

2) *Capacity Characterization*: After obtaining the decoding SNR of each $s_{ul,k}$ for $k = 1, 2$, the uplink achievable rate of user k can be calculated as $R_{ul,k}^{2 \rightarrow 1} = \log_2(1 + \gamma_{ul,k})$, i.e.,

$$R_{ul,1}^{2 \rightarrow 1} = \log_2(1 + \bar{\gamma}_{ul,1}\mathbf{g}_1), \quad (35)$$

$$R_{ul,2}^{2 \rightarrow 1} = \log_2\left(1 + \bar{\gamma}_{ul,2}\mathbf{g}_2\left(1 - \frac{\bar{\gamma}_{ul,1}\mathbf{g}_1|\rho|^2}{1 + \bar{\gamma}_{ul,1}\mathbf{g}_1}\right)\right). \quad (36)$$

Accordingly, the sum-rate capacity is calculated as follows:

$$\begin{aligned} C_{ul}^{2 \rightarrow 1} &= R_{ul,1}^{2 \rightarrow 1} + R_{ul,2}^{2 \rightarrow 1} \\ &= \log_2\left(1 + \bar{\gamma}_{ul,1}\bar{\gamma}_{ul,2}\mathbf{g}_1\mathbf{g}_2\bar{\rho} + \sum_{k=1}^2 \bar{\gamma}_{ul,k}\mathbf{g}_k\right), \end{aligned} \quad (37)$$

where $\bar{\rho} = 1 - |\rho|^2 \in [0, 1]$. Following the same derivation steps used to obtain (37), we can calculate the sum-rate capacity achieved under the SIC order $1 \rightarrow 2$ as follows.

Corollary 1. Under the SIC order $1 \rightarrow 2$, the achievable rates of user 1 and user 2, as well as the sum-rate capacity, can be expressed as follows:

$$R_{ul,1}^{1 \rightarrow 2} = \log_2\left(1 + \bar{\gamma}_{ul,1}\mathbf{g}_1\left(1 - \frac{\bar{\gamma}_{ul,2}\mathbf{g}_2|\rho|^2}{1 + \bar{\gamma}_{ul,2}\mathbf{g}_2}\right)\right), \quad (38)$$

$$R_{ul,2}^{1 \rightarrow 2} = \log_2(1 + \bar{\gamma}_{ul,2}\mathbf{g}_2), \quad (39)$$

$$C_{ul}^{1 \rightarrow 2} = \log_2\left(1 + \bar{\gamma}_{ul,1}\bar{\gamma}_{ul,2}\mathbf{g}_1\mathbf{g}_2\bar{\rho} + \sum_{k=1}^2 \bar{\gamma}_{ul,k}\mathbf{g}_k\right). \quad (40)$$

Comparing (37) with (40) yields the following conclusion.

Theorem 2. The sum-rate capacity of the considered uplink

CAPA-based channel is always the same, i.e.,

$$C_{ul} = \log_2 \left(1 + \bar{\gamma}_{ul,1} \bar{\gamma}_{ul,2} \mathbf{g}_1 \mathbf{g}_2 \bar{\rho} + \sum_{k=1}^2 \bar{\gamma}_{ul,k} \mathbf{g}_k \right), \quad (41)$$

regardless of the decoding order.

Remark 3. The sum-rate capacity expression given in (41) is determined by the *channel gain* of each user and the *channel correlation factor*. This expression is applicable to an arbitrary aperture *regardless of its location, shape, and size*. Furthermore, although only the LoS channel model is considered, the above derivations can be directly extended to other channel types, as they are *not channel-specific*.

Having obtained the sum-rate capacity, we now study the capacity region. The capacity region comprises all achievable rate pairs (R_1, R_2) , where R_k denotes the achievable rate of user $k \in \{1, 2\}$. The capacity region is defined by the rate pairs such that [2]

$$R_1 \leq \log_2(1 + \bar{\gamma}_{ul,1} \mathbf{g}_1), R_2 \leq \log_2(1 + \bar{\gamma}_{ul,2} \mathbf{g}_2), \quad (42)$$

$$R_1 + R_2 \leq \log_2 \left(1 + \bar{\gamma}_{ul,1} \bar{\gamma}_{ul,2} \mathbf{g}_1 \mathbf{g}_2 \bar{\rho} + \sum_{k=1}^2 \bar{\gamma}_{ul,k} \mathbf{g}_k \right). \quad (43)$$

This region can be achieved through SIC decoding along with time sharing, which forms a pentagon.

B. Downlink Capacity

In this part, we focus on the downlink scenario.

1) *Optimal Multiuser Precoding*: The capacity of a downlink multiuser Gaussian channel can be achieved using dirty-paper coding (DPC) [20]. We consider the encoding order $\varepsilon_K \rightarrow \varepsilon_{K-1} \rightarrow \dots \rightarrow \varepsilon_1$ with $\{\varepsilon_k\}_{k=1}^K = \{1, \dots, K\}$. For user ε_k , the dirty-paper encoder treats the interference from user $\varepsilon_{k'}$ for $k' > k$ as non-causally known, while its decoder regards the interference from user $\varepsilon_{k'}$ for $k' < k$ as additional noise. Let $V_{dl,k}(\mathbf{s})$ denote the detector used by user k to recover $s_{dl,k}$ from (7b). By applying DPC and using ML decoding at each user, the signal-to-noise-plus-interference ratio (SINR) for user ε_k is given by

$$\gamma_{dl,\varepsilon_k} = \frac{\bar{\mathbf{v}}_{\varepsilon_k} \left| \int_{\mathcal{A}} \mathbf{H}_{\varepsilon_k}(\mathbf{r}) \mathbf{J}_{dl,\varepsilon_k}(\mathbf{r}) d\mathbf{r} \right|^2}{\sigma_{\varepsilon_k}^2 \mathbf{v}_{\varepsilon_k} + \sum_{k' < k} \bar{\mathbf{v}}_{\varepsilon_{k'}} \left| \int_{\mathcal{A}} \mathbf{H}_{\varepsilon_{k'}}(\mathbf{r}) \mathbf{J}_{dl,\varepsilon_{k'}}(\mathbf{r}) d\mathbf{r} \right|^2}, \quad (44)$$

where $\mathbf{v}_{\varepsilon_k} = \int_{\mathcal{A}_{\varepsilon_k}} |V_{dl,\varepsilon_k}(\mathbf{s})|^2 d\mathbf{s}$ and $\bar{\mathbf{v}}_{\varepsilon_k} = \left| \int_{\mathcal{A}_{\varepsilon_k}} V_{dl,\varepsilon_k}^*(\mathbf{s}) d\mathbf{s} \right|^2$. Since each user's array aperture is negligible with respect to the propagation distance, we have

$$\bar{\mathbf{v}}_{\varepsilon_k} \approx |V_{dl,\varepsilon_k}(\mathbf{s}_{\varepsilon_k})|^2 A_{u,\varepsilon_k}^2, \mathbf{v}_{\varepsilon_k} \approx |V_{dl,\varepsilon_k}(\mathbf{s}_{\varepsilon_k})|^2 A_{u,\varepsilon_k}, \quad (45)$$

which simplifies $\gamma_{dl,\varepsilon_k}$ as follows:

$$\gamma_{dl,\varepsilon_k} \approx \frac{A_{u,\varepsilon_k} \left| \int_{\mathcal{A}} \mathbf{H}_{\varepsilon_k}(\mathbf{r}) \mathbf{J}_{dl,\varepsilon_k}(\mathbf{r}) d\mathbf{r} \right|^2}{\sigma_{\varepsilon_k}^2 + A_{u,\varepsilon_k} \sum_{k' < k} \left| \int_{\mathcal{A}} \mathbf{H}_{\varepsilon_{k'}}(\mathbf{r}) \mathbf{J}_{dl,\varepsilon_{k'}}(\mathbf{r}) d\mathbf{r} \right|^2}. \quad (46)$$

The sum-rate is given by $\sum_{k=1}^K \log_2(1 + \gamma_{dl,\varepsilon_k})$.

Under the two-user case, without loss of generality, we consider the DPC order $2 \rightarrow 1$. The achieved rates of user

1 and user 2 are given by

$$R_{dl,1}^{2 \rightarrow 1} = \log_2 \left(1 + \frac{A_{u,1} \left| \int_{\mathcal{A}} \mathbf{H}_1(\mathbf{r}) \mathbf{J}_{dl,1}(\mathbf{r}) d\mathbf{r} \right|^2}{\sigma_1^2} \right), \quad (47)$$

$$R_{dl,2}^{2 \rightarrow 1} = \log_2 \left(1 + \frac{A_{u,2} \left| \int_{\mathcal{A}} \mathbf{H}_2(\mathbf{r}) \mathbf{J}_{dl,2}(\mathbf{r}) d\mathbf{r} \right|^2}{\sigma_2^2 + A_{u,2} \left| \int_{\mathcal{A}} \mathbf{H}_2(\mathbf{r}) \mathbf{J}_{dl,1}(\mathbf{r}) d\mathbf{r} \right|^2} \right), \quad (48)$$

respectively. The problem of downlink sum-rate maximization is formulated as follows:

$$C_{dl}^{2 \rightarrow 1} = \max_{\sum_{k=1}^2 \int_{\mathcal{A}} |J_{dl,k}(\mathbf{r})|^2 d\mathbf{r} \leq P} R_{dl,1}^{2 \rightarrow 1} + R_{dl,2}^{2 \rightarrow 1}, \quad (49)$$

where P reflects the transmit power. Following the same derivation approach, the sum-rate achieved by the DPC order $1 \rightarrow 2$ can also be derived. For Gaussian channels, the maximal DPC sum-rate is independent of the DPC decoding order, and thus $C_{dl}^{2 \rightarrow 1}$ is essentially the downlink sum-rate capacity [21].

Problem (49) is non-convex, making the numerical identification of the maximum a nontrivial task. However, as demonstrated in [22], there exists a duality between the uplink and downlink scenarios. This duality establishes the equivalence of the DPC capacity region of a downlink channel with the capacity region of its dual uplink channel (as described in (24)), where users are subject to a sum power constraint. By defining $\bar{\gamma}_{du,k} \triangleq \frac{A_{u,k} k_0^2 \eta^2}{4\pi \sigma_k^2} P_k$ as the transmit SNRs of the dual uplink channel for $k = 1, 2$, the downlink sum-rate capacity is equal to the following dual uplink capacity [20]–[22]:

$$C_{du} = \max_{P_1, P_2 \geq 0, P_1 + P_2 \leq P} \log_2(1 + \bar{\gamma}_{du,1} \mathbf{g}_1 + \bar{\gamma}_{du,2} \mathbf{g}_2 + \bar{\gamma}_{du,1} \bar{\gamma}_{du,2} \mathbf{g}_1 \mathbf{g}_2 \bar{\rho}), \quad (50)$$

which is a convex problem and can be solved as follows.

Lemma 3. The optimal power allocation for the dual uplink is given by

$$(P_1^*, P_2^*) = \begin{cases} (P, 0) & \xi \geq P \\ (0, P) & \xi \leq -P \\ ((P - \xi)/2, (P + \xi)/2) & \text{else} \end{cases} \quad (51)$$

where $\xi = \frac{A_{u,1} \mathbf{g}_1 / \sigma_1^2 - A_{u,2} \mathbf{g}_2 / \sigma_2^2}{A_{u,1} A_{u,2} k_0^2 \eta^2 \mathbf{g}_1 \mathbf{g}_2 \bar{\rho} / (4\pi \sigma_1^2 \sigma_2^2)}$.

Proof: The results can be readily obtained by utilizing the Karush–Kuhn–Tucker (KKT) conditions. ■

Upon obtaining the optimal power allocation policy (51) for the dual uplink channel, we recover the corresponding downlink capacity-achieving source currents as follows.

Theorem 3. Given the DPC order $2 \rightarrow 1$ and the power constraint $\sum_{k=1}^2 \int_{\mathcal{A}} |J_{dl,k}(\mathbf{r})|^2 d\mathbf{r} \leq P$, the downlink capacity-achieving source currents for user 1 and user 2 are given by

$$\mathbf{J}_{dl,1}(\mathbf{r}) = \sqrt{P_1} \frac{\hat{\mathbf{H}}_1^*(\mathbf{r}) - \frac{P_2 \int_{\mathcal{A}} \hat{\mathbf{H}}_1^*(\mathbf{r}) \hat{\mathbf{H}}_2(\mathbf{r}) d\mathbf{r}}{1 + P_2 \int_{\mathcal{A}} |\hat{\mathbf{H}}_2(\mathbf{r})|^2 d\mathbf{r}} \hat{\mathbf{H}}_2^*(\mathbf{r})}{\sqrt{\int_{\mathcal{A}} |\hat{\mathbf{H}}_1(\mathbf{r})|^2 d\mathbf{r} - \frac{P_2 \left| \int_{\mathcal{A}} \hat{\mathbf{H}}_1^*(\mathbf{r}) \hat{\mathbf{H}}_2(\mathbf{r}) d\mathbf{r} \right|^2}{1 + P_2 \int_{\mathcal{A}} |\hat{\mathbf{H}}_2(\mathbf{r})|^2 d\mathbf{r}}}}, \quad (52)$$

$$\mathbf{J}_{dl,2}(\mathbf{r}) = \sqrt{P_2} \frac{\hat{\mathbf{H}}_2^*(\mathbf{r}) \sqrt{1 + \int_{\mathcal{A}} \hat{\mathbf{H}}_2(\mathbf{r}) \mathbf{J}_{dl,1}(\mathbf{r}) d\mathbf{r}}}{\int_{\mathcal{A}} |\hat{\mathbf{H}}_2(\mathbf{r})|^2 d\mathbf{r}}, \quad (53)$$

respectively, where $\hat{\mathbf{H}}_k(\mathbf{r}) = \frac{\sqrt{A_{u,k}}}{\sigma_k} \mathbf{H}_k(\mathbf{r})$ for $k =$

1: Encode the data information into the symbols $\{s_{dl,k}\}_{k=1}^2$ using DPC with the order $2 \rightarrow 1$;
2: Determine the dual power allocation policy $\{P_k\}_{k=1}^2$ according to the specific target quality of service requirements;
3: Generate the source current $J_{dl,1}(\mathbf{r})$:
$J_{dl,1}(\mathbf{r}) = \sqrt{P_1} \frac{\hat{H}_1^*(\mathbf{r}) - \frac{P_2 \int_{\mathcal{A}} \hat{H}_1^*(\mathbf{r}) \hat{H}_2(\mathbf{r}) d\mathbf{r}}{1 + P_2 \int_{\mathcal{A}} \hat{H}_2(\mathbf{r}) ^2 d\mathbf{r}} \hat{H}_2^*(\mathbf{r})}{\sqrt{\int_{\mathcal{A}} \hat{H}_1(\mathbf{r}) ^2 d\mathbf{r} - \frac{P_2 \int_{\mathcal{A}} \hat{H}_1^*(\mathbf{r}) \hat{H}_2(\mathbf{r}) d\mathbf{r} ^2}{1 + P_2 \int_{\mathcal{A}} \hat{H}_2(\mathbf{r}) ^2 d\mathbf{r}}}}$
4: Generate the source current $J_{dl,2}(\mathbf{r})$:
$J_{dl,2}(\mathbf{r}) = \sqrt{P_2} \frac{\hat{H}_2^*(\mathbf{r}) \sqrt{1 + \int_{\mathcal{A}} \hat{H}_2(\mathbf{r}) J_{dl,1}(\mathbf{r}) d\mathbf{r} ^2}}{\int_{\mathcal{A}} \hat{H}_2(\mathbf{r}) ^2 d\mathbf{r}}$
5: Formulate the transmit signal $x_{dl}(\mathbf{r}) = \sum_{k=1}^K J_{dl,k}(\mathbf{r}) s_{dl,k}$.

TABLE II: DPC-based precoding for downlink CAPA communications.

1,2. Additionally, the optimal source currents satisfy $\sum_{k=1}^2 \int_{\mathcal{A}} |J_{dl,k}(\mathbf{r})|^2 d\mathbf{r} = P_1 + P_2 = P$.

Proof: Please refer to Appendix D for more details. ■

Remark 4. Theorem 3 establishes the *uplink-to-downlink transformation* that takes as inputs an *uplink transmit power allocation policy* and an *SIC decoding order*, and outputs a set of *downlink source currents* with the same sum power as the uplink dual channel. As shown in Appendix D and Section IV-B2, the output source currents achieve the *same rates* as the dual uplink channel using the input power allocation policy and SIC decoding with the specified decoding order.

Having obtained the capacity-achieving source currents under the DPC order $2 \rightarrow 1$, we summarize the entire precoding procedure in Table II for ease of reference. The presented DPC procedure can be directly extended to the other order $1 \rightarrow 2$ by exchanging the user indices.

2) *Capacity Characterization:* As proved in Appendix D, given the power allocation policy (P_1, P_2) , the achievable rates of user 1 and user 2 under the DPC order $2 \rightarrow 1$ are given as follows:

$$R_{dl,1}^{2 \rightarrow 1} = \log_2 \left(1 + \bar{\gamma}_{dl,1} \mathbf{g}_1 \left(1 - \frac{\bar{\gamma}_{dl,2} \mathbf{g}_2 |\rho|^2}{1 + \bar{\gamma}_{dl,2} \mathbf{g}_2} \right) \right), \quad (54)$$

$$R_{dl,2}^{2 \rightarrow 1} = \log_2 (1 + \bar{\gamma}_{dl,2} \mathbf{g}_2). \quad (55)$$

By comparing the above two equations with the results in **Corollary 1**, the following observations are made.

Remark 5. The downlink user rates achieved by the DPC order $2 \rightarrow 1$ equal those achieved in the dual uplink channel under the SIC decoding order $1 \rightarrow 2$.

The achievable rates under the DPC order $1 \rightarrow 2$ can be derived with similar steps, which are omitted for brevity. For a thorough study, we derive the downlink-to-uplink transformation as follows.

Theorem 4. Given the source currents $\{J_{dl,k}(\mathbf{r})\}_{k=1}^2$ such that $\sum_{k=1}^2 \int_{\mathcal{A}} |J_{dl,k}(\mathbf{r})|^2 d\mathbf{r} \leq P$, the power allocation policy of the dual uplink channel, which achieves the same sum-rate as the

downlink channel under the DPC order $2 \rightarrow 1$, is given by

$$P_2 = \frac{|\int_{\mathcal{A}} \hat{H}_2(\mathbf{r}) J_{dl,2}(\mathbf{r}) d\mathbf{r}|^2}{\int_{\mathcal{A}} |\hat{H}_2(\mathbf{r})|^2 d\mathbf{r} (1 + |\int_{\mathcal{A}} \hat{H}_2(\mathbf{r}) J_{dl,1}(\mathbf{r}) d\mathbf{r}|^2)}, \quad (56)$$

$$P_1 = \frac{|\int_{\mathcal{A}} \hat{H}_1(\mathbf{r}) J_{dl,1}(\mathbf{r}) d\mathbf{r}|^2}{\int_{\mathcal{A}} |\hat{H}_1(\mathbf{r})|^2 d\mathbf{r} - \frac{P_2 |\int_{\mathcal{A}} \hat{H}_1^*(\mathbf{r}) \hat{H}_2(\mathbf{r}) d\mathbf{r}|^2}{1 + P_2 \int_{\mathcal{A}} |\hat{H}_2(\mathbf{r})|^2 d\mathbf{r}}}, \quad (57)$$

respectively, where $P_1 + P_2 \leq \sum_{k=1}^2 \int_{\mathcal{A}} |J_{dl,k}(\mathbf{r})|^2 d\mathbf{r} \leq P$.

Proof: Please refer to Appendix E for more details. ■

Remark 6. Theorem 4 establishes the *downlink-to-uplink transformation* which, given a set of *downlink source currents* and a *DPC encoding order*, outputs the *dual uplink power allocation policy* with the same sum power as the downlink currents. This policy achieves uplink rates (using SIC decoding) equal to the downlink rates.

Remark 7. The results in **Remark 4** and **Remark 6** suggest that under the same sum power constraint, the downlink DPC capacity region coincides with the capacity region of its dual uplink channel. This further verifies the existence of uplink-downlink duality in CAPA communications.

In light of the uplink-downlink duality, the sum-rate downlink capacity remains constant regardless of the DPC order (similar to its dual uplink channel), and is given as follows.

Theorem 5. The sum-rate capacity of the downlink CAPA-based two-user channel is given by

$$C_{dl} = \log_2 \left(1 + \bar{\gamma}_{dl,1} \bar{\gamma}_{dl,2} \mathbf{g}_1 \mathbf{g}_2 \bar{\rho} + \sum_{k=1}^2 \bar{\gamma}_{dl,k} \mathbf{g}_k \right) \quad (58a)$$

$$= \begin{cases} \log_2 (1 + \bar{\gamma}_{dl,1}(\mathbf{P}) \mathbf{g}_1) & \xi \geq \mathbf{P} \\ \log_2 (1 + \bar{\gamma}_{dl,2}(\mathbf{P}) \mathbf{g}_2) & \xi \leq -\mathbf{P} \\ \log_2 (1 + \varepsilon_1 + \varepsilon_2 + \varepsilon_1 \varepsilon_2 \bar{\rho}) & \text{else} \end{cases}, \quad (58b)$$

where $\bar{\gamma}_{dl,k}(x) \triangleq \frac{A_{u,k} k \sigma_0^2 \eta^2}{4\pi \sigma_k^2} x$ for $k = 1, 2$, $\varepsilon_1 = \bar{\gamma}_{dl,1}(\frac{\mathbf{P}-\xi}{2}) \mathbf{g}_1$, and $\varepsilon_2 = \bar{\gamma}_{dl,2}(\frac{\mathbf{P}+\xi}{2}) \mathbf{g}_2$.

Proof: Eq. (58) is obtained by inserting (51) into (50). ■

Remark 8. The downlink sum-rate capacity given in (58) is determined by the channel gain of each user and the channel correlation factor. This expression is applicable to an arbitrary aperture, regardless of its location, shape, and size.

Furthermore, according to the uplink-downlink duality, given a power allocation scheme (P_1, P_2) with $P_1 + P_2 = P$, we can obtain the capacity region of a dual uplink channel. The downlink capacity region is the convex hull of the union of all these dual uplink capacity regions, which is illustrated in Section VI.

V. CASE STUDIES

As discussed in **Remark 3** and **Remark 8**, the sum-rate capacity expressions derived for both uplink and downlink CAPA communications are applicable to apertures of arbitrary location, shape, and size, among other factors. In the following sections, we specialize \mathcal{A} to several specific cases to unveil more system insights.

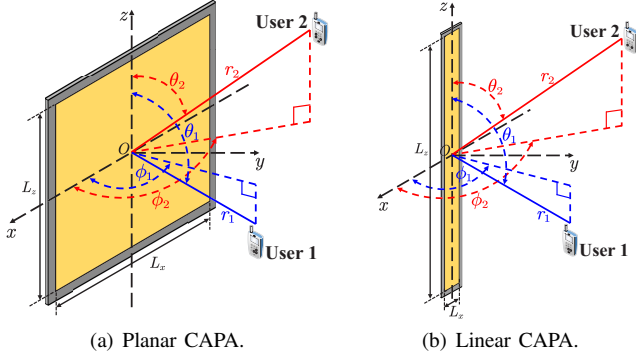


Fig. 2: Geometries of CAPAs.

A. Planar CAPAs

We first consider the case where the BS array is a planar CAPA placed on the x - z plane and centered at the origin, as shown in Fig. 2(a). The edges of \mathcal{A} are parallel to the axes, with physical dimensions L_x and L_z along the x - and z -axes, respectively. In this case, we have $\mathcal{A} = \{[x, 0, z]^T | x \in [-\frac{L_x}{2}, \frac{L_x}{2}], z \in [-\frac{L_z}{2}, \frac{L_z}{2}]\}$. For each user $k \in \{1, 2\}$, let r_k represent the distance from the center of \mathcal{A} to the center of \mathcal{A}_k , $\phi_k \in [0, \pi]$ and $\theta_k \in [0, \pi]$ denote the associated azimuth and elevation angles, respectively. Consequently, $\mathbf{s}_k = [r_k \Phi_k, r_k \Psi_k, r_k \Theta_k]^T$, where $\Phi_k \triangleq \cos \phi_k \sin \theta_k$, $\Psi_k \triangleq \sin \phi_k \sin \theta_k$, and $\Theta_k \triangleq \cos \theta_k$. Based on (8) and (15), for $\mathbf{r} = [x, 0, z]^T \in \mathcal{A}$, we have

$$\mathbf{g}_k(\mathbf{r}) = \frac{\sqrt{r_k \Psi_k} e^{-jk_0(x^2+z^2-2r_k(\Phi_k x + \Theta_k z) + r_k^2)} \frac{1}{2}}{\sqrt{4\pi}(x^2+z^2-2r_k(\Phi_k x + \Theta_k z) + r_k^2)^{\frac{3}{4}}} \triangleq \mathbf{Q}_k(x, z). \quad (59)$$

To characterize the capacity, we derive closed-form expressions of the channel gain and correlation factor as follows.

Lemma 4. With the planar CAPA, the channel gain for each user can be calculated as follows:

$$\mathbf{g}_k = \frac{1}{4\pi} \sum_{x \in \mathcal{X}_k} \sum_{z \in \mathcal{Z}_k} \arctan \left(\frac{xz/\Psi_k}{\sqrt{\Psi_k^2 + x^2 + z^2}} \right) \triangleq \mathbf{g}_k^p, \quad (60)$$

where $k \in \{1, 2\}$, $\mathcal{X}_k \triangleq \{\frac{L_x}{2r_k} \pm \Phi_k\}$, and $\mathcal{Z}_k \triangleq \{\frac{L_z}{2r_k} \pm \Theta_k\}$. The associated channel correlation factor is approximated by

$$\rho = \frac{\pi^2 A}{4n^2 \sqrt{\mathbf{g}_1^p \mathbf{g}_2^p}} \sum_{j=1}^n \sum_{j'=1}^n \sqrt{(1-\psi_j^2)(1-\psi_{j'}^2)} \times \mathbf{Q}_1^* \left(\frac{L_x \psi_j}{2}, \frac{L_z \psi_{j'}}{2} \right) \mathbf{Q}_2 \left(\frac{L_x \psi_j}{2}, \frac{L_z \psi_{j'}}{2} \right) \triangleq \rho_p, \quad (61)$$

where n is a complexity-vs-accuracy tradeoff parameter, and $\psi_j = \cos \left(\frac{(2j-1)\pi}{2n} \right)$ for $j \in \{1, \dots, n\}$.

Proof: Please refer to Appendix F for more details. ■

Subsequently, the closed-form expressions of sum-rate capacity can be readily obtained.

Corollary 2. The sum-rate capacity for the planar CAPA-based two-user channel can be written as follows:

$$C_i = \log_2 \left(1 + \bar{\gamma}_{i,1} \mathbf{g}_1^p + \bar{\gamma}_{i,2} \mathbf{g}_2^p + \bar{\gamma}_{i,1} \bar{\gamma}_{i,2} \mathbf{g}_1^p \mathbf{g}_2^p \bar{\rho}_p \right), \quad (62)$$

where $i \in \{\text{ul}, \text{dl}\}$, and $\bar{\rho}_p = 1 - |\rho_p|^2 \in [0, 1]$.

To shed more light on the characteristics of planar CAPAs, we investigate the asymptotic sum-rate capacity for a limiting case where \mathcal{A} is assumed to be infinitely large, i.e., $L_x, L_z \rightarrow \infty$. In this case, we have $\lim_{L_x, L_z \rightarrow \infty} \mathbf{g}_k^p = \frac{1}{4\pi} \frac{4\pi}{2} = \frac{1}{2}$. Regarding $\lim_{L_x, L_z \rightarrow \infty} \rho_p$, while it is computationally intractable, based on the numerical results presented in [23], [24], we observe that $\lim_{L_x, L_z \rightarrow \infty} \rho_p \ll 1$. Taken together, we can obtain the asymptotic sum-rate capacity as follows:

$$\lim_{L_x, L_z \rightarrow \infty} C_i \approx \log_2(1 + \bar{\gamma}_{i,1}/2) + \log_2(1 + \bar{\gamma}_{i,2}/2), \quad (63)$$

where $i \in \{\text{ul}, \text{dl}\}$. The results in (63) suggest that when the BS is equipped with an infinitely large planar CAPA, half of the transmission power of each user can be captured by the receiver, and the inter-user interference vanishes.

Remark 9. The above observation makes intuitive sense because an infinitely large planar CAPA can receive at most half of the power transmitted by an isotropic source, while the other half of the power will never reach the surface.

B. Linear CAPAs

Next, we simplify the planar CAPA to a linear CAPA with $L_x \ll L_z$. In this case, the variations in currents and channel responses across the x -axis within \mathcal{A} are negligible. The channel gain and correlation factor are calculated as follows.

Lemma 5. The channel gain for the linear CAPA is given by

$$\mathbf{g}_k = \frac{L_x \sin \phi_k \varrho_k}{4\pi r_k \sin \theta_k}, \quad (64)$$

where $\varrho_k = \frac{L_z - 2r_k \Theta_k}{(L_z^2 - 4r_k \Theta_k L_z + 4r_k^2)^{\frac{1}{2}}} + \frac{L_z + 2r_k \Theta_k}{(L_z^2 + 4r_k \Theta_k L_z + 4r_k^2)^{\frac{1}{2}}}$. The channel correlation factor satisfies

$$\rho = \frac{\pi L_z}{2n} \sum_{j=1}^n \sqrt{1 - \psi_j^2} \mathbf{Q}_1^* \left(0, \frac{L_z \psi_j}{2} \right) \mathbf{Q}_2 \left(0, \frac{L_z \psi_j}{2} \right). \quad (65)$$

Proof: When $L_x \ll L_z$, we have $\mathbf{g}_k \approx L_x \int_{-\frac{L_z}{2}}^{\frac{L_z}{2}} |\mathbf{Q}_k(0, z)|^2 dz$ and $\rho \approx L_x \int_{-\frac{L_z}{2}}^{\frac{L_z}{2}} \mathbf{Q}_1^*(0, z) \mathbf{Q}_2(0, z) dz$. The subsequent derivation steps are similar to those shown in Appendix F, and the final results follow immediately. ■

When the linear CAPA is infinitely long, i.e., $L_z \rightarrow \infty$, the asymptotic sum-rate capacity satisfies

$$\lim_{L_z \rightarrow \infty} C_i \approx \sum_{k=1}^2 \log_2 \left(1 + \frac{L_x \sin \phi_i \bar{\gamma}_{i,k}}{2\pi r_k \sin \theta_k} \right), \quad (66)$$

where $i \in \{\text{ul}, \text{dl}\}$. By comparing (63) with (66), we observe that the asymptotic sum-rate capacity achieved by the linear CAPA is influenced not only by the transmit SNR but also by the locations of the users, which is in contrast to the planar CAPA.

C. Planar SPDAs

Finally, we consider a case where the above planar CAPA is partitioned into $M = M_z M_x$ spatially discrete elements, where $M_x = 2\bar{M}_x + 1$ and $M_z = 2\bar{M}_z + 1$ denote the number of antenna elements along the x - and z -axes, as depicted in Fig. 3. The physical dimensions of each element are indicated by $\sqrt{A_s}$, and the inter-element distance is denoted as d , where $\sqrt{A_s} \leq d \ll r_k$. In this case, the central position of

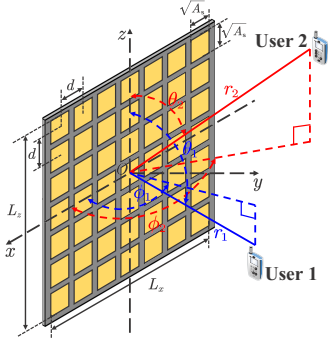


Fig. 3: Planar SPDA.

each element is given by $[m_x d, 0, m_z d]^T$ for $m_x \in \mathcal{M}_x \triangleq \{0, \pm 1, \dots, \pm M_x\}$ and $m_z \in \mathcal{M}_z \triangleq \{0, \pm 1, \dots, \pm M_z\}$. Further, we have $L_x \approx M_x d$, $L_z \approx M_z d$, and $\mathcal{A} = \{[m_x d + \ell_x, 0, m_z d + \ell_z]^T | \ell_x, \ell_z \in [-\frac{\sqrt{A_s}}{2}, \frac{\sqrt{A_s}}{2}], m_x \in \mathcal{M}_x, m_z \in \mathcal{M}_z\}$.

Lemma 6. The channel gain and channel correlation factor for the planar SPDA satisfy $\mathbf{g}_k^s = \zeta_{oc} \mathbf{g}_k^p$ and $\rho_s = A_s \sum_{m_x \in \mathcal{M}_x} \sum_{m_z \in \mathcal{M}_z} Q_1^*(m_x d, m_z d) Q_2(m_x d, m_z d)$, respectively, where $\zeta_{oc} \triangleq \frac{A_s}{d^2} \in (0, 1]$ is defined as the array occupation ratio.

Proof: Please refer to Appendix G for more details. ■

Therefore, the asymptotic sum-rate capacity achieved by the planar SPDA is given by

$$\lim_{M_x, M_z \rightarrow \infty} C_i \approx \sum_{k=1}^2 \log_2(1 + \zeta_{oc} \bar{\gamma}_{i,k}/2), \quad (67)$$

where $i \in \{\text{ul}, \text{dl}\}$. Comparing (63) with (67) yields the following observations.

Remark 10. The capacity achieved by an SPDA increases to that achieved by a CAPA when $\zeta_{oc} = 1$. This makes intuitive sense as an SPDA turns into a CAPA when the array occupation ratio equals one.

VI. NUMERICAL RESULTS

In this section, computer simulations are performed to demonstrate the performance of CAPA communications and verify the accuracy of the developed analytical results. For clarity, the simulations employ the planar arrays specified in Section V. Unless otherwise specified, the simulation parameters are set as follows: $\lambda = 0.0107$ m, $d = \frac{\lambda}{2}$, $A_{u,1} = A_{u,2} = \frac{\lambda^2}{4\pi}$, $L_x = L_z$, $M_x = M_z$, $\bar{\gamma}_{\text{ul},1} = 30$ dB, $\bar{\gamma}_{\text{ul},2} = 40$ dB, $\bar{\gamma}_{\text{dl},1} + \bar{\gamma}_{\text{dl},2} = 50$ dB with $\sigma_1^2 = \sigma_2^2$, $\theta_1 = \theta_2 = \frac{\pi}{6}$, $\phi_1 = \phi_2 = \frac{\pi}{3}$, $r_1 = 10$ m, and $r_2 = 20$ m. All the results are calculated by setting the complexity-vs-accuracy tradeoff parameter n as $n = 200$.

A. Uplink CAPA Communications

Fig. 4 illustrates the uplink per-user rate and sum-rate capacity achieved by the CAPA in terms of the BS aperture size under the SIC decoding orders $1 \rightarrow 2$ and $2 \rightarrow 1$. It can be observed from this graph that as the aperture size A grows, all the presented rates increase. This increase is attributed to the larger aperture size enhancing channel gain

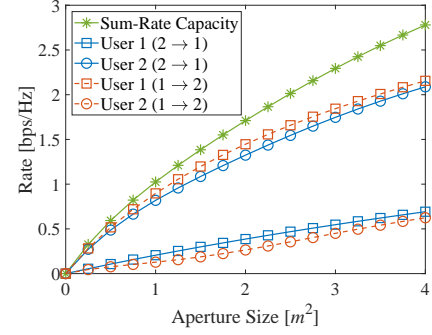


Fig. 4: Uplink transmission rates achieved by CAPA.

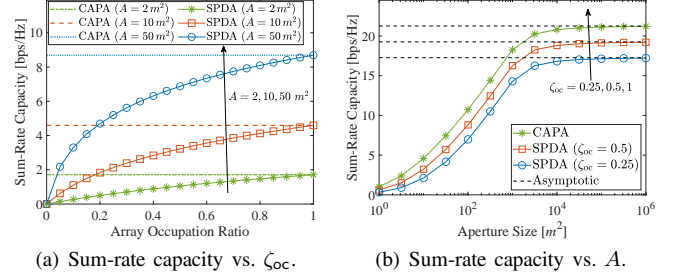
(a) Sum-rate capacity vs. ζ_{oc} .(b) Sum-rate capacity vs. A .

Fig. 5: Uplink sum-rate capacity.

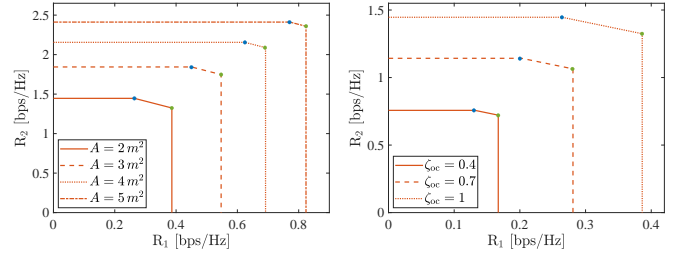
(a) Capacity region vs. A (b) Capacity region vs. ζ_{oc} , $A = 2 \text{ m}^2$.

Fig. 6: Uplink capacity regions.

and reducing channel correlation, which in turn enhances the dedicated signal and diminishes the IUI, as discussed in (63).

To compare the performance gap between CAPA and the conventional SPDA in terms of sum-rate capacity, we plot the sum-rate capacity for SPDAs as a function of the array occupation ratio ζ_{oc} in Fig. 5(a). As shown in the graph, the sum-rate capacity for an SPDA gradually converges with that of a CAPA as the array occupation ratio increases towards 1. This observation validates the statements in **Remark 10**. Additionally, the results in Fig. 5(a) indicate that increasing the aperture size can boost the channel capacity. To gain further insights into the capacity limit as the BS aperture size A approaches infinity, we plot the sum-rate capacity against the aperture size in Fig. 5(b). As anticipated, increasing the aperture size causes the sum-rate capacity to approach its upper bound, as derived in (63) and (67). It is worth mentioning that the asymptotic sum-rate capacity for an infinitely large aperture is a finite value, subject to the principle of energy conservation [23]. This verifies our discussions in **Remark 9**.

Fig. 6 shows the uplink capacity region achieved by the CAPA, where the green and blue points represent the achieved rates by SIC decoding order $1 \rightarrow 2$ and $2 \rightarrow 1$, respectively. The rate tuple on the line segment connecting these two points

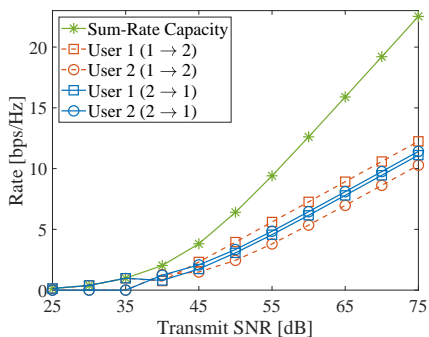
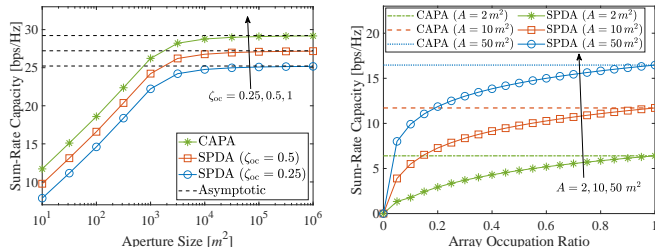


Fig. 7: Downlink transmission rates achieved by CAPA.



(a) Sum-rate capacity vs. A . (b) Sum-rate capacity vs. ζ_{oc} .

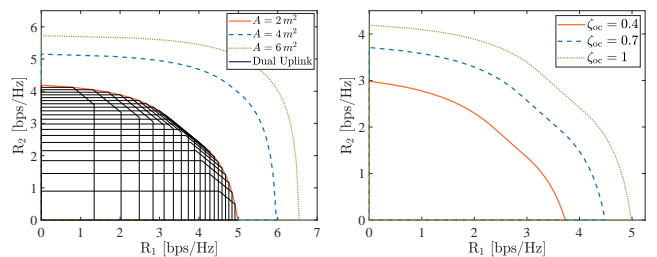
Fig. 8: Downlink sum-rate capacity.

is achieved by the *time-sharing strategy*. In Fig. 6(a), the capacity regions achieved by the CAPA for various aperture sizes are illustrated. It can be observed that the capacity region expands with increasing A , shifting from a pentagonal to a rectangular shape. This phenomenon occurs because the IUI decreases as the aperture size increases, which is consistent with the results shown in Fig. 4. Furthermore, as depicted in Fig. 6(b), the capacity region of the CAPA surpasses that of the SPDA, and their disparity narrows as the array occupation rate ζ_{oc} increases, reinforcing findings from Fig. 5(a). These findings underscore the superiority of CAPAs over conventional SPDAs in terms of channel capacity.

B. Downlink CAPA Communications

Fig. 7 plots the per-user rate and the sum-rate capacity in terms of the total transmit SNR $\bar{\gamma}_{dl,1} + \bar{\gamma}_{dl,2}$ in downlink CAPA communications. It is observed that the transmission rates of both users exhibit identical high-SNR slopes, regardless of the DPC encoding orders. Fig. 8(a) and Fig. 8(b) illustrate the downlink sum-rate capacity with respect to the aperture size and array occupation ratio, respectively. Similar to the uplink case, the downlink sum-rate capacity converges to its upper bound as the aperture size increases. Additionally, for the SPDA, the achieved sum-rate capacity is positively correlated with the array occupation ratio, further suggesting that the CAPA outperforms the SPDA in terms of channel capacity.

Fig. 9 illustrates the downlink capacity region achieved by the CAPA. The downlink capacity region is depicted by the convex hull of all the corresponding dual uplink capacity regions with the same sum power budget [20]. This means that the boundary of the downlink capacity region is formed by the corner points of the dual uplink capacity regions, as illustrated in Fig. 9(a). It is observed that the downlink capacity region of



(a) CAPA capacity region vs. A . (b) Capacity region vs. ζ_{oc} , $A = 2 m^2$

Fig. 9: Downlink capacity regions.

the CAPA expands with the aperture size A , whereas the capacity region of the SPDA expands with the array occupation ratio ζ_{oc} . Taken together, these observations demonstrate that the CAPA achieves a more extensive downlink capacity region than the conventional SPDA, highlighting its superiority.

VII. CONCLUSION

This article has proposed an analytically tractable framework for CAPA-based wireless communications by utilizing continuous operators to address the continuous nature of the EM field. This framework significantly differs from the conventional matrix-based transmission framework for SPDA-based communications. Based on this novel framework, we have characterized the capacity limits of uplink and downlink channels for CAPAs in both single-user and multiuser cases. For each investigated scenario, we derived closed-form expressions for the capacity-achieving detectors or source currents along with the corresponding capacity. Additionally, we have analyzed the channel capacity by specializing the derived results to several typical array structures. Through both theoretical analyses and numerical simulations, we have demonstrated that CAPA exhibits a higher sum-rate capacity and a more extensive capacity region compared to the conventional SPDA. This underscores CAPA's potential as a promising transmission paradigm for future wireless networks.

APPENDIX

A. Proof of Lemma 1

The mean of $\int_{\mathcal{A}} \mathbf{V}_{ul}^*(\mathbf{r}) \mathbf{N}_{ul}(\mathbf{r}) d\mathbf{r}$ is calculated as follows:

$$\mathbb{E} \left\{ \int_{\mathcal{A}} \mathbf{V}_{ul}^*(\mathbf{r}) \mathbf{N}_{ul}(\mathbf{r}) d\mathbf{r} \right\} = \int_{\mathcal{A}} \mathbf{V}_{ul}^*(\mathbf{r}) \mathbb{E} \{ \mathbf{N}_{ul}(\mathbf{r}) \} d\mathbf{r}, \quad (\text{A1})$$

which, together with the fact that $\mathbb{E} \{ \mathbf{N}_{ul}(\mathbf{r}) \} = 0$, yields $\mathbb{E} \left\{ \int_{\mathcal{A}} \mathbf{V}_{ul}^*(\mathbf{r}) \mathbf{N}_{ul}(\mathbf{r}) d\mathbf{r} \right\} = 0$. The variance is given by

$$\mathbb{E} \left\{ \int_{\mathcal{A}} \mathbf{V}_{ul}^*(\mathbf{r}) \mathbf{N}_{ul}(\mathbf{r}) d\mathbf{r} \int_{\mathcal{A}} \mathbf{V}_{ul}(\mathbf{r}') \mathbf{N}_{ul}^*(\mathbf{r}') d\mathbf{r}' \right\} \quad (\text{A2})$$

$$= \int_{\mathcal{A}} \int_{\mathcal{A}} \mathbf{V}_{ul}^*(\mathbf{r}) \mathbf{V}_{ul}(\mathbf{r}') \mathbb{E} \{ \mathbf{N}_{ul}(\mathbf{r}) \mathbf{N}_{ul}^*(\mathbf{r}') \} d\mathbf{r} d\mathbf{r}' \quad (\text{A3})$$

$$= \int_{\mathcal{A}} \mathbf{V}_{ul}(\mathbf{r}') \int_{\mathcal{A}} \mathbf{V}_{ul}^*(\mathbf{r}) \sigma^2 \delta(\mathbf{r} - \mathbf{r}') d\mathbf{r} d\mathbf{r}' \quad (\text{A4})$$

$$\stackrel{\clubsuit}{=} \int_{\mathcal{A}} \mathbf{V}_{ul}(\mathbf{r}') (\sigma^2 \mathbf{V}_{ul}^*(\mathbf{r}')) d\mathbf{r}' = \sigma^2 \int_{\mathcal{A}} |\mathbf{V}_{ul}(\mathbf{r})|^2 d\mathbf{r}, \quad (\text{A5})$$

where the step ♣ is based on the fact that $\int_{\mathcal{A}} \delta(\mathbf{x} - \mathbf{x}_0) f(\mathbf{x}) d\mathbf{x} = f(\mathbf{x}_0)$ with $f(\cdot)$ being an arbitrary function defined on \mathcal{A} .

B. Proof of Lemma 2

Firstly, we prove that the autocorrelation function of $Z_w(\mathbf{r})$ satisfies $\mathbb{E}\{Z_w(\mathbf{r})Z_w^*(\mathbf{r}')\} = \sigma^2\delta(\mathbf{r} - \mathbf{r}')$. Specifically, $\mathbb{E}\{Z_w(\mathbf{r})Z_w^*(\mathbf{r}')\}$ can be calculated as follows:

$$\begin{aligned} & \mathbb{E}\{Z_w(\mathbf{r})Z_w^*(\mathbf{r}')\} \\ &= \int_{\mathcal{A}} \int_{\mathcal{A}} W_Z(\mathbf{r}, \mathbf{x}) W_Z^*(\mathbf{r}', \mathbf{x}') \mathbb{E}\{Z(\mathbf{x})Z^*(\mathbf{x}')\} d\mathbf{x} d\mathbf{x}' \quad (\text{A6}) \\ &= \int_{\mathcal{A}} W_Z^*(\mathbf{r}', \mathbf{x}') \int_{\mathcal{A}} W_Z(\mathbf{r}, \mathbf{x}) R_Z(\mathbf{x}, \mathbf{x}') d\mathbf{x} d\mathbf{x}'. \quad (\text{A7}) \end{aligned}$$

By substituting (27) and (30) into (A7) and then calculating the inner integral with respect to \mathbf{x} , we obtain

$$\begin{aligned} & \int_{\mathcal{A}} W_Z(\mathbf{r}, \mathbf{x}) R_Z(\mathbf{x}, \mathbf{x}') d\mathbf{x} = \sigma^2(\delta(\mathbf{r} - \mathbf{x}') \\ & + (\bar{\gamma}_{ul,1} + \mu_1 + \mu_1 \bar{\gamma}_{ul,1} \mathbf{g}_1) G_1(\mathbf{r}) G_1^*(\mathbf{x}')). \quad (\text{A8}) \end{aligned}$$

By continuously substituting (A8) and (30) into (A7), we next calculate the outer integral in terms of \mathbf{x}' , which yields

$$\begin{aligned} & \mathbb{E}\{Z_w(\mathbf{r})Z_w^*(\mathbf{r}')\} = \sigma^2(\delta(\mathbf{r} - \mathbf{r}') + G_1(\mathbf{r})G_1^*(\mathbf{r}') \\ & \times (2\mu_1 + \bar{\gamma}_{ul,1} + 2\mu_1 \bar{\gamma}_{ul,1} \mathbf{g}_1 + \mu_1^2 \mathbf{g}_1 + \bar{\gamma}_{ul,1} \mu_1^2 \mathbf{g}_1^2)). \quad (\text{A9}) \end{aligned}$$

With $\mu_1 = -\frac{1}{\mathbf{g}_1} \pm \frac{1}{\mathbf{g}_1 \sqrt{1 + \bar{\gamma}_{ul,1} \mathbf{g}_1}}$, it is readily shown that

$$2\mu_1 + \bar{\gamma}_{ul,1} + 2\mu_1 \bar{\gamma}_{ul,1} \mathbf{g}_1 + \mu_1^2 \mathbf{g}_1 + \bar{\gamma}_{ul,1} \mu_1^2 \mathbf{g}_1^2 = 0. \quad (\text{A10})$$

Therefore, we have $\mathbb{E}\{Z_w(\mathbf{r})Z_w^*(\mathbf{r}')\} = \sigma^2\delta(\mathbf{r} - \mathbf{r}')$.

Next, we prove that $W_Z(\mathbf{r}', \mathbf{r})$ is an invertible linear transformation. We define

$$\bar{W}_Z(\mathbf{r}, \mathbf{r}') \triangleq \delta(\mathbf{r} - \mathbf{r}') - \frac{\mu_1}{1 + \mu_1 \mathbf{g}_1} G_1(\mathbf{r}) G_1^*(\mathbf{r}'). \quad (\text{A11})$$

For an arbitrary function $f(\mathbf{r})$ defined in $\mathbf{r} \in \mathcal{A}$, we have

$$\begin{aligned} & \int_{\mathcal{A}} \bar{W}_Z(\mathbf{x}, \mathbf{r}') \int_{\mathcal{A}} W_Z(\mathbf{r}', \mathbf{r}) f(\mathbf{r}) d\mathbf{r} d\mathbf{r}' \\ &= \int_{\mathcal{A}} f(\mathbf{r}) \int_{\mathcal{A}} \bar{W}_Z(\mathbf{x}, \mathbf{r}') W_Z(\mathbf{r}', \mathbf{r}) d\mathbf{r}' d\mathbf{r}. \quad (\text{A12}) \end{aligned}$$

By inserting (30) and (A11) into (A12) and utilizing the fact that $\int_{\mathcal{A}} \delta(\mathbf{x} - \mathbf{x}_0) f(\mathbf{x}) d\mathbf{x} = f(\mathbf{x}_0)$, we calculate the inner integral in terms of \mathbf{r}' as follows:

$$\begin{aligned} & \int_{\mathcal{A}} \bar{W}_Z(\mathbf{x}, \mathbf{r}') W_Z(\mathbf{r}', \mathbf{r}) d\mathbf{r}' = \delta(\mathbf{x} - \mathbf{r}) + G_1(\mathbf{x}) \\ & \times G_1^*(\mathbf{r}) \left(\mu_1 - \frac{\mu_1 + \mu_1^2 \mathbf{g}_1}{1 + \mu_1 \mathbf{g}_1} \right) = \delta(\mathbf{x} - \mathbf{r}). \quad (\text{A13}) \end{aligned}$$

Plugging (A13) into (A12) gives

$$\begin{aligned} & \int_{\mathcal{A}} \bar{W}_Z(\mathbf{x}, \mathbf{r}') \int_{\mathcal{A}} W_Z(\mathbf{r}', \mathbf{r}) f(\mathbf{r}) d\mathbf{r} d\mathbf{r}' \\ &= \int_{\mathcal{A}} f(\mathbf{r}) \delta(\mathbf{x} - \mathbf{r}) d\mathbf{r} = f(\mathbf{x}), \quad (\text{A14}) \end{aligned}$$

which suggests that the inversion of $W_Z(\mathbf{r}', \mathbf{r})$ is $\bar{W}_Z(\mathbf{r}, \mathbf{r}')$.

C. Proof of Theorem 1

By definition, $\bar{H}_2(\mathbf{r}')$ can be calculated as follows:

$$\bar{H}_2(\mathbf{r}') = \int_{\mathcal{A}} (\delta(\mathbf{r}' - \mathbf{r}) + \mu_1 G_1(\mathbf{r}') G_1^*(\mathbf{r})) H_2(\mathbf{r}) d\mathbf{r} \quad (\text{A15})$$

$$= jk_0 \eta / \sqrt{4\pi} (G_2(\mathbf{r}') + \mu_1 \sqrt{\mathbf{g}_1 \mathbf{g}_2} \rho G_1(\mathbf{r}')). \quad (\text{A16})$$

Inserting (A16) into (33) yields

$$\gamma_{ul,2} = \bar{\gamma}_{ul,2} \int_{\mathcal{A}} |G_2(\mathbf{r}') + \mu_1 \sqrt{\mathbf{g}_1 \mathbf{g}_2} \rho G_1(\mathbf{r}')|^2 d\mathbf{r}' \quad (\text{A17})$$

$$\begin{aligned} &= \bar{\gamma}_{ul,2} \int_{\mathcal{A}} |G_2(\mathbf{r}')|^2 d\mathbf{r}' + \bar{\gamma}_{ul,2} \mu_1^2 \mathbf{g}_1 \mathbf{g}_2 |\rho|^2 \int_{\mathcal{A}} |G_1(\mathbf{r}')|^2 d\mathbf{r}' \\ &+ 2\bar{\gamma}_{ul,2} \mu_1 \sqrt{\mathbf{g}_1 \mathbf{g}_2} \Re \left\{ \rho \int_{\mathcal{A}} G_1(\mathbf{r}') G_2^*(\mathbf{r}') d\mathbf{r}' \right\} \quad (\text{A18}) \end{aligned}$$

$$= \bar{\gamma}_{ul,2} \mathbf{g}_2 (1 + \mathbf{g}_1 |\rho|^2 \mu_1 (\mu_1 \mathbf{g}_1 + 2)). \quad (\text{A19})$$

Furthermore, based on (A10), we have

$$\mu_1 (\mu_1 \mathbf{g}_1 + 2) = -\bar{\gamma}_{ul,1} (1 + \mu_1 \mathbf{g}_1)^2, \quad (\text{A20})$$

which, together with (A19), yields

$$\gamma_{ul,2} = \bar{\gamma}_{ul,2} \mathbf{g}_2 (1 - \bar{\gamma}_{ul,1} \mathbf{g}_1 |\rho|^2 (1 + \mu_1 \mathbf{g}_1)^2). \quad (\text{A21})$$

Plugging $\mu_1 = -\frac{1}{\mathbf{g}_1} \pm \frac{1}{\mathbf{g}_1 \sqrt{1 + \bar{\gamma}_{ul,1} \mathbf{g}_1}}$ into (A21) gives

$$\gamma_{ul,2} = \bar{\gamma}_{ul,2} \mathbf{g}_2 \left(1 - \frac{\bar{\gamma}_{ul,1} \mathbf{g}_1 |\rho|^2}{1 + \bar{\gamma}_{ul,1} \mathbf{g}_1} \right). \quad (\text{A22})$$

The final results follow immediately.

D. Proof of Theorem 3

Our objective is to verify that the presented source current distributions $\{J_{dl,k}(\mathbf{r})\}_{k=1}^2$ are able to: i) achieve the downlink sum-rate capacity $\log_2(1 + \bar{\gamma}_{dl,1} \mathbf{g}_1 + \bar{\gamma}_{dl,2} \mathbf{g}_2 + \bar{\gamma}_{dl,1} \bar{\gamma}_{dl,2} \mathbf{g}_1 \mathbf{g}_2 \bar{\rho})$, and ii) satisfy the sum power constraint $\sum_{k=1}^2 \int_{\mathcal{A}} |J_{dl,k}(\mathbf{r})|^2 d\mathbf{r} = P_1 + P_2 = P$.

Substituting (52) into $|\int_{\mathcal{A}} \hat{H}_1(\mathbf{r}) J_{dl,1}(\mathbf{r}) d\mathbf{r}|^2$ gives

$$\begin{aligned} & \left| \int_{\mathcal{A}} \hat{H}_1(\mathbf{r}) J_{dl,1}(\mathbf{r}) d\mathbf{r} \right|^2 = \frac{P_1 P_2 \left| \int_{\mathcal{A}} \hat{H}_1^*(\mathbf{r}) \hat{H}_2(\mathbf{r}) d\mathbf{r} \right|^2}{-1 - P_2 \int_{\mathcal{A}} |\hat{H}_2(\mathbf{r})|^2 d\mathbf{r}} \\ & + P_1 \int_{\mathcal{A}} |\hat{H}_1(\mathbf{r})|^2 d\mathbf{r} = \bar{\gamma}_{dl,1} \mathbf{g}_1 \left(1 - \frac{\bar{\gamma}_{dl,2} \mathbf{g}_2 |\rho|^2}{1 + \bar{\gamma}_{dl,2} \mathbf{g}_2} \right), \quad (\text{A23}) \end{aligned}$$

which yields

$$R_{dl,1}^{2 \rightarrow 1} = \log_2 \left(1 + \left| \int_{\mathcal{A}} \hat{H}_1(\mathbf{r}) J_{dl,1}(\mathbf{r}) d\mathbf{r} \right|^2 \right) \quad (\text{A24})$$

$$= \log_2 \left(1 + \bar{\gamma}_{dl,1} \mathbf{g}_1 \left(1 - \frac{\bar{\gamma}_{dl,2} \mathbf{g}_2 |\rho|^2}{1 + \bar{\gamma}_{dl,2} \mathbf{g}_2} \right) \right). \quad (\text{A25})$$

Moreover, inserting (53) into (48) gives

$$R_{dl,2}^{2 \rightarrow 1} = \log_2 \left(1 + \frac{\left| \int_{\mathcal{A}} \hat{H}_2(\mathbf{r}) J_{dl,2}(\mathbf{r}) d\mathbf{r} \right|^2}{1 + \left| \int_{\mathcal{A}} \hat{H}_2(\mathbf{r}) J_{dl,1}(\mathbf{r}) d\mathbf{r} \right|^2} \right) \quad (\text{A26})$$

$$= \log_2 \left(1 + P_2 \frac{\int_{\mathcal{A}} |\hat{H}_2(\mathbf{r})|^2 d\mathbf{r}}{\int_{\mathcal{A}} |\hat{H}_2(\mathbf{r})|^2 d\mathbf{r}} \right) \quad (\text{A27})$$

$$= \log_2 (1 + \bar{\gamma}_{dl,2} \mathbf{g}_2). \quad (\text{A28})$$

Inserting (A25) and (A28) into $R_{dl,1}^{2 \rightarrow 1} + R_{dl,2}^{2 \rightarrow 1}$ gives the sum-rate capacity for a given (P_1, P_2) , i.e., $\log_2(1 + \bar{\gamma}_{dl,1} \mathbf{g}_1 +$

$\bar{\gamma}_{dl,2}g_2 + \bar{\gamma}_{dl,1}\bar{\gamma}_{dl,2}g_1g_2\bar{\rho}$), which concludes the proof of the first part.

We next turn to the sum power constraint. Note that

$$\int_{\mathcal{A}} |J_{dl,1}(\mathbf{r})|^2 d\mathbf{r} = \int_{\mathcal{A}} \int_{\mathcal{A}} J_{dl,1}(\mathbf{r}) \delta(\mathbf{r} - \mathbf{r}') J_{dl,1}^*(\mathbf{r}') d\mathbf{r} d\mathbf{r}'. \quad (\text{A29})$$

On the other hand, based on (53), $\int_{\mathcal{A}} |J_{dl,2}(\mathbf{r})|^2 d\mathbf{r}$ can be calculated as follows:

$$\int_{\mathcal{A}} |J_{dl,2}(\mathbf{r})|^2 d\mathbf{r} = P_2 + P_2 \left| \int_{\mathcal{A}} \hat{H}_2(\mathbf{r}) J_{dl,1}(\mathbf{r}) d\mathbf{r} \right|^2 \quad (\text{A30})$$

$$= P_2 + P_2 \int_{\mathcal{A}} \int_{\mathcal{A}} J_{dl,1}(\mathbf{r}) \hat{H}_2(\mathbf{r}) \hat{H}_2^*(\mathbf{r}') J_{dl,1}^*(\mathbf{r}') d\mathbf{r} d\mathbf{r}'. \quad (\text{A31})$$

The sum of (A29) and (A31) satisfies

$$\sum_{k=1}^2 \int_{\mathcal{A}} |J_{dl,k}(\mathbf{r})|^2 d\mathbf{r} = P_2 + \int_{\mathcal{A}} \int_{\mathcal{A}} J_{dl,1}(\mathbf{r}) (\delta(\mathbf{r} - \mathbf{r}') + P_2 \hat{H}_2(\mathbf{r}) \hat{H}_2^*(\mathbf{r}')) J_{dl,1}^*(\mathbf{r}') d\mathbf{r} d\mathbf{r}'. \quad (\text{A32})$$

Substituting (52) into (A32) yields

$$\begin{aligned} & \int_{\mathcal{A}} \int_{\mathcal{A}} J_{dl,1}(\mathbf{r}) (\delta(\mathbf{r} - \mathbf{r}') + P_2 \hat{H}_2(\mathbf{r}) \hat{H}_2^*(\mathbf{r}')) d\mathbf{r} J_{dl,1}^*(\mathbf{r}') d\mathbf{r}' \\ &= P_1 \frac{\int_{\mathcal{A}} \int_{\mathcal{A}} f_n(\mathbf{r}) (\delta(\mathbf{r} - \mathbf{r}') + P_2 \hat{H}_2(\mathbf{r}) \hat{H}_2^*(\mathbf{r}')) d\mathbf{r} f_n^*(\mathbf{r}') d\mathbf{r}'}{\int_{\mathcal{A}} |\hat{H}_1(\mathbf{r})|^2 d\mathbf{r} - \frac{P_2 \int_{\mathcal{A}} \hat{H}_1^*(\mathbf{r}) \hat{H}_2(\mathbf{r}) d\mathbf{r}}{1 + P_2 \int_{\mathcal{A}} |\hat{H}_2(\mathbf{r})|^2 d\mathbf{r}}}, \end{aligned} \quad (\text{A33})$$

where $f_n(\mathbf{r}) \triangleq \hat{H}_1^*(\mathbf{r}) - \frac{P_2 \int_{\mathcal{A}} \hat{H}_1^*(\mathbf{r}) \hat{H}_2(\mathbf{r}) d\mathbf{r}}{1 + P_2 \int_{\mathcal{A}} |\hat{H}_2(\mathbf{r})|^2 d\mathbf{r}} \hat{H}_2^*(\mathbf{r})$. The inner integral in the numerator of (A33) can be calculated as follows:

$$\int_{\mathcal{A}} f_n(\mathbf{r}) (\delta(\mathbf{r} - \mathbf{r}') + P_2 \hat{H}_2(\mathbf{r}) \hat{H}_2^*(\mathbf{r}')) d\mathbf{r} \quad (\text{A34})$$

$$\begin{aligned} &= \hat{H}_1^*(\mathbf{r}') + \left(1 - \frac{1 + P_2 \int_{\mathcal{A}} |\hat{H}_2(\mathbf{r})|^2 d\mathbf{r}}{1 + P_2 \int_{\mathcal{A}} |\hat{H}_2(\mathbf{r})|^2 d\mathbf{r}} \right) \\ &\times P_2 \left(\int_{\mathcal{A}} \hat{H}_1^*(\mathbf{r}) \hat{H}_2(\mathbf{r}) d\mathbf{r} \right) \hat{H}_2^*(\mathbf{r}') = \hat{H}_1^*(\mathbf{r}'), \end{aligned} \quad (\text{A35})$$

based on which the outer integral in the numerator of (A33) is calculated as follows:

$$\int_{\mathcal{A}} \hat{H}_1^*(\mathbf{r}') f_n^*(\mathbf{r}') d\mathbf{r}' = -\frac{P_2 \int_{\mathcal{A}} \hat{H}_1^*(\mathbf{r}) \hat{H}_2(\mathbf{r}) d\mathbf{r}}{1 + P_2 \int_{\mathcal{A}} |\hat{H}_2(\mathbf{r})|^2 d\mathbf{r}} + \int_{\mathcal{A}} |\hat{H}_1(\mathbf{r})|^2 d\mathbf{r}. \quad (\text{A36})$$

As a result, we obtain

$$(\text{A33}) = P_1 \frac{\int_{\mathcal{A}} |\hat{H}_1(\mathbf{r})|^2 d\mathbf{r} - \frac{P_2 \int_{\mathcal{A}} \hat{H}_1^*(\mathbf{r}) \hat{H}_2(\mathbf{r}) d\mathbf{r}}{1 + P_2 \int_{\mathcal{A}} |\hat{H}_2(\mathbf{r})|^2 d\mathbf{r}}}{\int_{\mathcal{A}} |\hat{H}_1(\mathbf{r})|^2 d\mathbf{r} - \frac{P_2 \int_{\mathcal{A}} \hat{H}_1^*(\mathbf{r}) \hat{H}_2(\mathbf{r}) d\mathbf{r}}{1 + P_2 \int_{\mathcal{A}} |\hat{H}_2(\mathbf{r})|^2 d\mathbf{r}}} = P_1, \quad (\text{A37})$$

which, together with (A32), suggests that $\sum_{k=1}^2 \int_{\mathcal{A}} |J_{dl,k}(\mathbf{r})|^2 d\mathbf{r} = P_1 + P_2$. As the downlink sum-rate equals that of its dual uplink channel under the same sum power constraint, the downlink capacity is achieved when the CAPA transmits at maximum power, i.e., $P_1 + P_2 = P$, which concludes the proof of the second part.

E. Proof of Theorem 4

Our objective is to verify that the presented power allocation policy (P_1, P_2) is able to: i) ensure the uplink rates equal the

downlink rates shown in (47) and (48), and ii) satisfy the sum power constraint $P_1 + P_2 \leq \sum_{k=1}^2 \int_{\mathcal{A}} |J_{dl,k}(\mathbf{r})|^2 d\mathbf{r} \leq P$. The first part can be directly proved by substituting (56) and (57) into (54) and (55). We next turn to the sum power constraint.

Following the derivation steps in Appendix B, it is proved that the inversion of $U(\mathbf{r}', \mathbf{r})$ is $\bar{U}(\mathbf{r}, \mathbf{r}')$, where $U(\mathbf{r}', \mathbf{r}) = \delta(\mathbf{r}' - \mathbf{r}) + \mu_2 G_2(\mathbf{r}') G_2^*(\mathbf{r})$ with $\mu_2 = -\frac{1}{g_2} \pm \frac{1}{g_2 \sqrt{1 + \bar{\gamma}_{dl,2} g_2}}$ and $\bar{U}(\mathbf{r}, \mathbf{r}') = \delta(\mathbf{r} - \mathbf{r}') - \frac{\mu_2}{1 + \mu_2 g_2} G_2(\mathbf{r}) G_2^*(\mathbf{r}')$, i.e., $\int_{\mathcal{A}} \bar{U}(\mathbf{r}, \mathbf{x}) U(\mathbf{x}, \mathbf{r}') d\mathbf{x} = \int_{\mathcal{A}} U(\mathbf{r}, \mathbf{x}) \bar{U}(\mathbf{x}, \mathbf{r}') d\mathbf{x} = \delta(\mathbf{r} - \mathbf{r}')$. Furthermore, it is worth noting that $\int_{\mathcal{A}} \hat{H}_1(\mathbf{r}) J_{dl,1}(\mathbf{r}) d\mathbf{r} = \int_{\mathcal{A}} \int_{\mathcal{A}} \hat{H}_1(\mathbf{r}') \delta(\mathbf{r}' - \mathbf{r}) J_{dl,1}(\mathbf{r}) d\mathbf{r}' d\mathbf{r} \triangleq \diamond$. It follows that

$$\begin{aligned} \diamond &= \int_{\mathcal{A}} \int_{\mathcal{A}} \int_{\mathcal{A}} \hat{H}_1(\mathbf{r}') U(\mathbf{r}', \mathbf{x}) \bar{U}(\mathbf{x}, \mathbf{r}) J_{dl,1}(\mathbf{r}) d\mathbf{r} d\mathbf{x} d\mathbf{r}' \\ &= \int_{\mathcal{A}} \int_{\mathcal{A}} \hat{H}_1(\mathbf{r}') U(\mathbf{r}', \mathbf{x}) d\mathbf{r}' \int_{\mathcal{A}} \bar{U}(\mathbf{x}, \mathbf{r}) J_{dl,1}(\mathbf{r}) d\mathbf{r} d\mathbf{x}, \end{aligned} \quad (\text{A38})$$

which, together with the Cauchy's inequality, yields

$$|\diamond|^2 \leq \int_{\mathcal{A}} |\diamond_1(\mathbf{x})|^2 d\mathbf{x} \int_{\mathcal{A}} |\diamond_2(\mathbf{x})|^2 d\mathbf{x}, \quad (\text{A39})$$

where $\diamond_1(\mathbf{x}) \triangleq \int_{\mathcal{A}} \bar{U}(\mathbf{x}, \mathbf{r}) J_{dl,1}(\mathbf{r}) d\mathbf{r} = J_{dl,1}(\mathbf{x}) - \frac{\mu_2 G_2^*(\mathbf{x})}{1 + \mu_2 g_2} \int_{\mathcal{A}} G_2(\mathbf{r}) J_{dl,1}(\mathbf{r}) d\mathbf{r}$ and $\diamond_2(\mathbf{x}) \triangleq \int_{\mathcal{A}} \hat{H}_1(\mathbf{r}') U(\mathbf{r}', \mathbf{x}) d\mathbf{r}' = \mu_2 G_2(\mathbf{x}) \int_{\mathcal{A}} G_2^*(\mathbf{r}') \hat{H}_1(\mathbf{r}') d\mathbf{r}' + \hat{H}_1(\mathbf{x})$. Consequently, we have

$$\begin{aligned} & \int_{\mathcal{A}} |\diamond_2(\mathbf{x})|^2 d\mathbf{x} = \int_{\mathcal{A}} |\hat{H}_1(\mathbf{x})|^2 d\mathbf{x} + \left| \int_{\mathcal{A}} G_2^*(\mathbf{r}') \hat{H}_1(\mathbf{r}') d\mathbf{r}' \right|^2 \\ & \times (2\mu_2 + \mu_2^2 g_2) = \int_{\mathcal{A}} |\hat{H}_1(\mathbf{x})|^2 d\mathbf{x} - \frac{\left| \int_{\mathcal{A}} G_2(\mathbf{r}') \hat{H}_1^*(\mathbf{r}') d\mathbf{r}' \right|^2}{(1 + \bar{\gamma}_{dl,2} g_2) / \bar{\gamma}_{dl,2}} \\ & = \int_{\mathcal{A}} |\hat{H}_1(\mathbf{r})|^2 d\mathbf{r} - \frac{P_2 \left| \int_{\mathcal{A}} \hat{H}_1^*(\mathbf{r}) \hat{H}_2(\mathbf{r}) d\mathbf{r} \right|^2}{1 + P_2 \int_{\mathcal{A}} |\hat{H}_2(\mathbf{r})|^2 d\mathbf{r}}, \end{aligned} \quad (\text{A40})$$

which, together with (57) and (A39), yields $P_1 \leq \int_{\mathcal{A}} |\diamond_1(\mathbf{x})|^2 d\mathbf{x}$. Furthermore, we obtain

$$\begin{aligned} & \int_{\mathcal{A}} |\diamond_1(\mathbf{x})|^2 d\mathbf{x} = \int_{\mathcal{A}} |J_{dl,1}(\mathbf{r})|^2 d\mathbf{r} - \left| \int_{\mathcal{A}} G_2(\mathbf{r}) J_{dl,1}(\mathbf{r}) d\mathbf{r} \right|^2 \\ & \times \left(\frac{2\mu_2}{1 + \mu_2 g_2} - \left(\frac{\mu_2}{1 + \mu_2 g_2} \right)^2 g_2 \right). \end{aligned} \quad (\text{A41})$$

Recalling that $\mu_2 = -\frac{1}{g_2} \pm \frac{1}{g_2 \sqrt{1 + \bar{\gamma}_{dl,2} g_2}}$ yields $\frac{2\mu_2}{1 + \mu_2 g_2} - \left(\frac{\mu_2}{1 + \mu_2 g_2} \right)^2 g_2 = -\bar{\gamma}_{dl,2}$, which yields

$$\int_{\mathcal{A}} |\diamond_1(\mathbf{x})|^2 d\mathbf{x} = \int_{\mathcal{A}} |J_{dl,1}(\mathbf{r})|^2 d\mathbf{r} + P_2 \left| \int_{\mathcal{A}} \hat{H}_2(\mathbf{r}) J_{dl,1}(\mathbf{r}) d\mathbf{r} \right|^2.$$

As proved above, we have $P_1 \leq \int_{\mathcal{A}} |\diamond_1(\mathbf{x})|^2 d\mathbf{x}$, and thus the powers satisfy

$$P_1 + P_2 \leq \int_{\mathcal{A}} |J_{dl,1}(\mathbf{r})|^2 d\mathbf{r} + P_2 \left(1 + \left| \int_{\mathcal{A}} \hat{H}_2(\mathbf{r}) J_{dl,1}(\mathbf{r}) d\mathbf{r} \right|^2 \right), \quad (\text{A42})$$

which, together with (56), yields

$$\begin{aligned} P_1 + P_2 &\leq \int_{\mathcal{A}} |J_{dl,1}(\mathbf{r})|^2 d\mathbf{r} + \frac{\left| \int_{\mathcal{A}} \hat{H}_2(\mathbf{r}) J_{dl,2}(\mathbf{r}) d\mathbf{r} \right|^2}{\int_{\mathcal{A}} |\hat{H}_2(\mathbf{r})|^2 d\mathbf{r}}, \\ &\stackrel{\heartsuit}{\leq} \int_{\mathcal{A}} |J_{dl,1}(\mathbf{r})|^2 d\mathbf{r} + \int_{\mathcal{A}} |J_{dl,2}(\mathbf{r})|^2 d\mathbf{r} \leq P, \end{aligned} \quad (\text{A43})$$

where the step \heartsuit in (A43) is due to the Cauchy's inequality.

This completes the proof of **Theorem 4**.

F. Proof of Lemma 4

Based on (59), the channel gain for the planar CAPA can be calculated as follows:

$$\begin{aligned} g_k &= \int_{-\frac{L_x}{2}}^{\frac{L_x}{2}} \int_{-\frac{L_z}{2}}^{\frac{L_z}{2}} \mathbf{Q}_k^*(x, z) \mathbf{Q}_k(x, z) dx dz = \frac{r_k \Psi_k}{4\pi} \int_{-\frac{L_x}{2}}^{\frac{L_x}{2}} \\ &\times \int_{-\frac{L_z}{2}}^{\frac{L_z}{2}} (x^2 + z^2 - 2r_k (\Phi_k x + \Theta_k z) + r_k^2)^{-\frac{3}{2}} dx dz. \end{aligned}$$

Subsequently, we can calculate the inner integral with the aid of [25, Eq. (2.264.5)] and the outer integral with the aid of [25, Eq. (2.284)], which yields the results in (60). The channel correlation factor can be written as follows:

$$\rho = \int_{-\frac{L_x}{2}}^{\frac{L_x}{2}} \int_{-\frac{L_z}{2}}^{\frac{L_z}{2}} \mathbf{Q}_1^*(x, z) \mathbf{Q}_2(x, z) dx dz. \quad (\text{A44})$$

The above integrals can be calculated by applying the Chebyshev-Gauss quadrature rule, i.e., $\int_{-1}^1 \frac{f(x)}{\sqrt{1-x^2}} dx \approx \sum_{j=1}^n f(x_j)$ with $x_j = \cos\left(\frac{(2j-1)\pi}{2n}\right)$, lead to the results in (61). This completes the proof of **Lemma 4**.

G. Proof of Lemma 6

In the case of an planar SPDA, due to the small element size compared to the distance between the BS and the user, i.e., $\sqrt{A_s} \ll r_k$, the variation of the channel across an element is negligible. Thus, the channel gain can be written as follows:

$$g_k = \sum_{m_x \in \mathcal{M}_x} \sum_{m_z \in \mathcal{M}_z} A_s |\mathbf{Q}_k(m_x d, m_z d)|^2. \quad (\text{A45})$$

Defining $\epsilon_k = \frac{d}{r_k} \ll 1$, we can rewrite (A45) as follows:

$$g_k = \frac{A \Psi_k}{4\pi r_k^2} \sum_{m_x \in \mathcal{M}_x} \sum_{m_z \in \mathcal{M}_z} f_{\text{sp}}^{(k)}(m_x \epsilon_k, m_z \epsilon_k), \quad (\text{A46})$$

where $f_{\text{sp}}^{(k)}(x, z) \triangleq (x^2 + z^2 - 2\Phi_k x - 2\Theta_k z + 1)^{-\frac{3}{2}}$ is defined within the square area $\mathcal{C}_k \triangleq \{(x, z) \mid -\frac{M_x \epsilon_k}{2} \leq x \leq \frac{M_x \epsilon_k}{2}, -\frac{M_z \epsilon_k}{2} \leq z \leq \frac{M_z \epsilon_k}{2}\}$, which is then divided into $M_x M_z$ sub-squares, each with an area ϵ_k^2 . As $\epsilon_k \ll 1$, we have $f_{\text{sp}}^{(k)}(x, z) \approx f_{\text{sp}}^{(k)}(m_x \epsilon_k, m_z \epsilon_k)$ for $\forall (x, z) \in \{(x, z) \mid (m_x - \frac{1}{2}) \epsilon_k \leq x \leq (m_x + \frac{1}{2}) \epsilon_k, (m_z - \frac{1}{2}) \epsilon_k \leq z \leq (m_z + \frac{1}{2}) \epsilon_k\}$. It follows from the concept of double integral that

$$\sum_{m_x \in \mathcal{M}_x} \sum_{m_z \in \mathcal{M}_z} f_{\text{sp}}^{(k)}(m_x \epsilon_k, m_z \epsilon_k) \epsilon_k^2 \approx \iint_{\mathcal{C}_k} f_{\text{sp}}^{(k)}(x, z) dx dz.$$

Consequently, (A46) can be rewritten as follows:

$$g_k \approx \frac{\zeta_{\text{oc}} \Psi_k}{4\pi} \int_{-\frac{M_z \epsilon_k}{2}}^{\frac{M_z \epsilon_k}{2}} \int_{-\frac{M_x \epsilon_k}{2}}^{\frac{M_x \epsilon_k}{2}} f_{\text{sp}}^{(k)}(x, z) dx dz, \quad (\text{A47})$$

which can be calculated by utilizing [25, Eqs. (2.264.5) & (2.284)]. Furthermore, the expression of ρ_s follows from its definition, which completes the entire proof.

REFERENCES

- [1] C. Ouyang, Y. Liu, and X. Zhang, "On the performance of continuous aperture array (CAPA)-based wireless communications," *arXiv preprint arXiv:2405.16690*, 2024.
- [2] D. Tse and P. Viswanath, *Fundamentals of Wireless Communication*. Cambridge, U.K.: Cambridge Univ. Press, 2005.
- [3] Y. Liu *et al.*, "Near-field communications: A tutorial review," *IEEE Open J. Commun. Soc.*, vol. 4, pp. 1999–2049, 2023.
- [4] C. Huang *et al.*, "Holographic MIMO surfaces for 6G wireless networks: Opportunities, challenges, and trends," *IEEE Wireless Commun.*, vol. 27, no. 5, pp. 118–125, Oct. 2020.
- [5] O. T. Demir *et al.*, "Channel modeling and channel estimation for holographic massive MIMO with planar arrays," *IEEE Wireless Commun. Lett.*, vol. 11, no. 5, pp. 997–1001, May 2022.
- [6] A. Pizzo, T. L. Marzetta, and L. Sanguinetti, "Spatially-stationary model for holographic MIMO small-scale fading," *IEEE J. Sel. Areas Commun.*, vol. 38, no. 9, pp. 1964–1979, Sep. 2020.
- [7] C. Liaskos *et al.*, "A new wireless communication paradigm through software-controlled metasurfaces," *IEEE Commun. Mag.*, vol. 56, no. 9, pp. 162–169, Sep. 2018.
- [8] Y. Liu *et al.*, "Near-field communications: A comprehensive survey," *arXiv preprint arXiv:2401.05900*, 2024.
- [9] M. D. Migliore, "On electromagnetics and information theory," *IEEE Trans. Antennas Propag.*, vol. 56, no. 10, pp. 3188–3200, Oct. 2008.
- [10] —, "Horse (electromagnetics) is more important than horseman (information) for wireless transmission," *IEEE Trans. Antennas Propag.*, vol. 67, no. 4, pp. 2046–2055, Apr. 2019.
- [11] M. A. Jensen and J. W. Wallace, "Capacity of the continuous-space electromagnetic channel," *IEEE Trans. Antennas Propag.*, vol. 56, no. 2, pp. 524–531, Feb. 2008.
- [12] Z. Xie, Y. Liu, J. Xu, X. Wu, and A. Nallanathan, "Performance analysis for near-field MIMO: Discrete and continuous aperture antennas," *IEEE Wireless Commun. Lett.*, vol. 12, no. 12, pp. 2258–2262, Dec. 2023.
- [13] R. Deng, Y. Zhang, H. Zhang, B. Di, H. Zhang, H. V. Poor, and L. Song, "Reconfigurable holographic surfaces for ultra-massive MIMO in 6G: Practical design, optimization and implementation," *IEEE J. Sel. Areas Commun.*, vol. 41, no. 8, pp. 2367–2379, Aug. 2023.
- [14] L. Sanguinetti, A. A. D'Amico, and M. Debbah, "Wavenumber-division multiplexing in line-of-sight holographic MIMO communications," *IEEE Trans. Wireless Commun.*, vol. 22, no. 4, pp. 2186–2201, Apr. 2023.
- [15] W. Jeon and S.-Y. Chung, "Capacity of continuous-space electromagnetic channels with lossy transceivers," *IEEE Trans. Inf. Theory*, vol. 64, no. 3, pp. 1977–1991, Mar. 2018.
- [16] J. Xu, X. Mu, and Y. Liu, "Exploiting STAR-RISs in near-field communications," *IEEE Trans. Wireless Commun.*, vol. 22, no. 3, pp. 2181–2196, Mar. 2024.
- [17] C. A. Balanis, *Antenna Theory: Analysis and Design*. Hoboken, NJ, USA: Wiley, 2016.
- [18] F. K. Gruber and E. A. Marengo, "New aspects of electromagnetic information theory for wireless and antenna systems," *IEEE Trans. Antennas Propagat.*, vol. 56, no. 11, pp. 3470–3484, Nov. 2008.
- [19] C. Ouyang, Z. Wang, B. Zhao, Y. Liu, and X. Zhang, "On the impact of reactive region on the near-field channel gain," *arXiv preprint arXiv:2404.08343*, 2024.
- [20] A. Goldsmith, S. Jafar, N. Jindal, and S. Vishwanath, "Capacity limits of MIMO channels," *IEEE J. Sel. Areas Commun.*, vol. 21, no. 5, pp. 684–702, Jun. 2003.
- [21] A. El Gamal and Y.-H. Kim, *Network Information Theory*. New York, NY, USA: Cambridge Univ. Press, 2011.
- [22] S. Vishwanath, N. Jindal, and A. Goldsmith, "Duality, achievable rates, and sum-rate capacity of Gaussian MIMO broadcast channels," *IEEE Trans. Inf. Theory*, vol. 49, no. 10, pp. 2658–2668, Oct. 2003.
- [23] B. Zhao, C. Ouyang, Y. Liu, X. Zhang, and H. V. Poor, "Modeling and analysis of near-field ISAC," *IEEE J. Sel. Top. Signal Process.*, pp. 1–16, Early Access, 2024.
- [24] Y. Liu, C. Ouyang, Z. Ding, and R. Schober, "The road to next-generation multiple access: A 50-year tutorial review," *arXiv preprint arXiv:2403.00189*, 2024.
- [25] I. S. Gradshteyn and I. M. Ryzhik, *Table of Integrals, Series and Products*, 7th ed. New York, NY, USA: Academic Press, 2007.